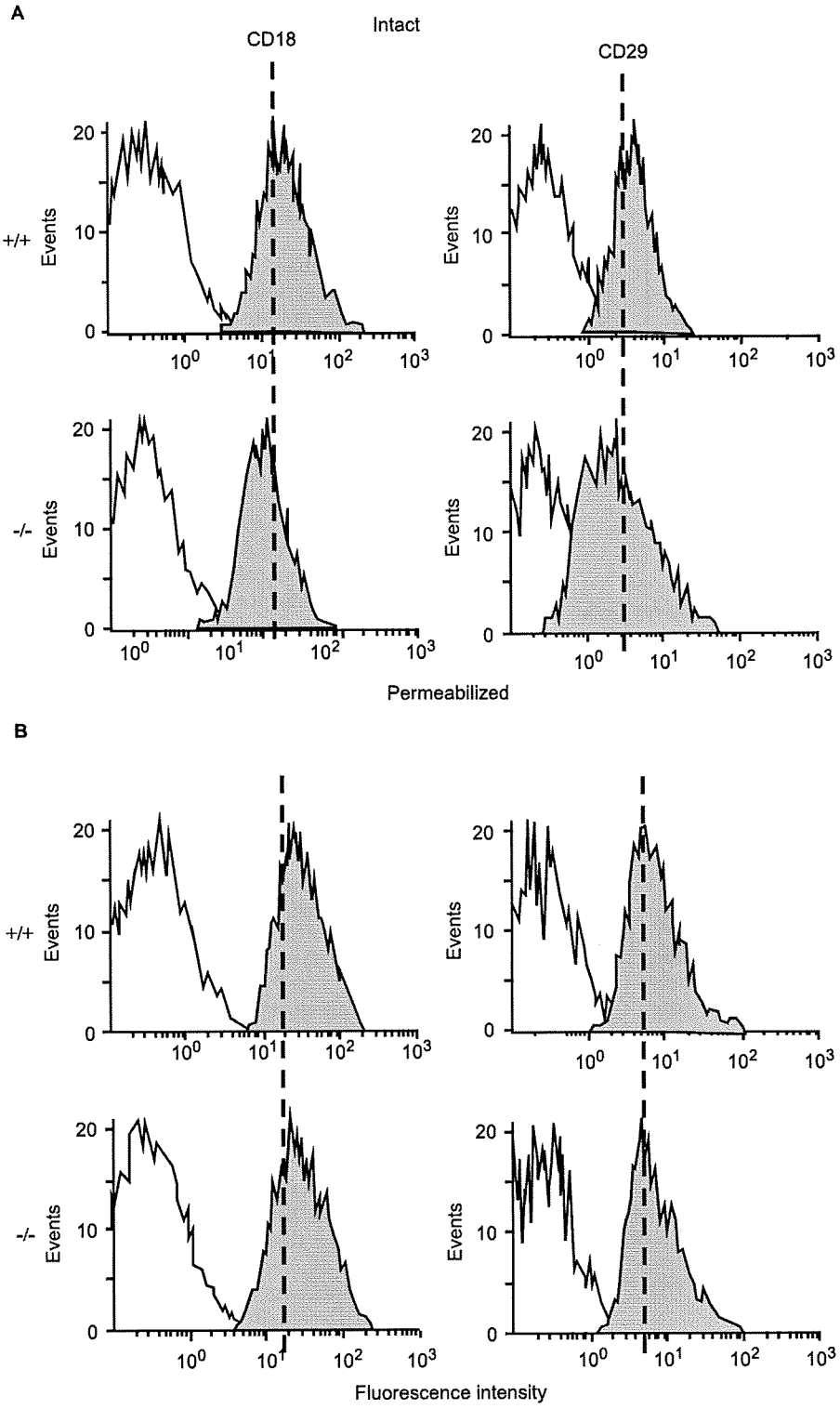

Fig. 4. **Expression levels of CD18 and CD29 in wild-type or *CatE*$^{-/-}$ macrophages.** (A) Macrophages (2×10^5 cells) from wild-type and *CatE*$^{-/-}$ mice were stained for the cell surface with specific antibodies for CD18 and CD29, subsequently treated with FITC-labelled second antibodies and then analysed by flow cytometry. Data are representative of five independent experiments. (B) The cells were permeabilized with saponin and then stained for determination of the total expression levels of CD18 or CD29. Data are representative five of independent experiments.

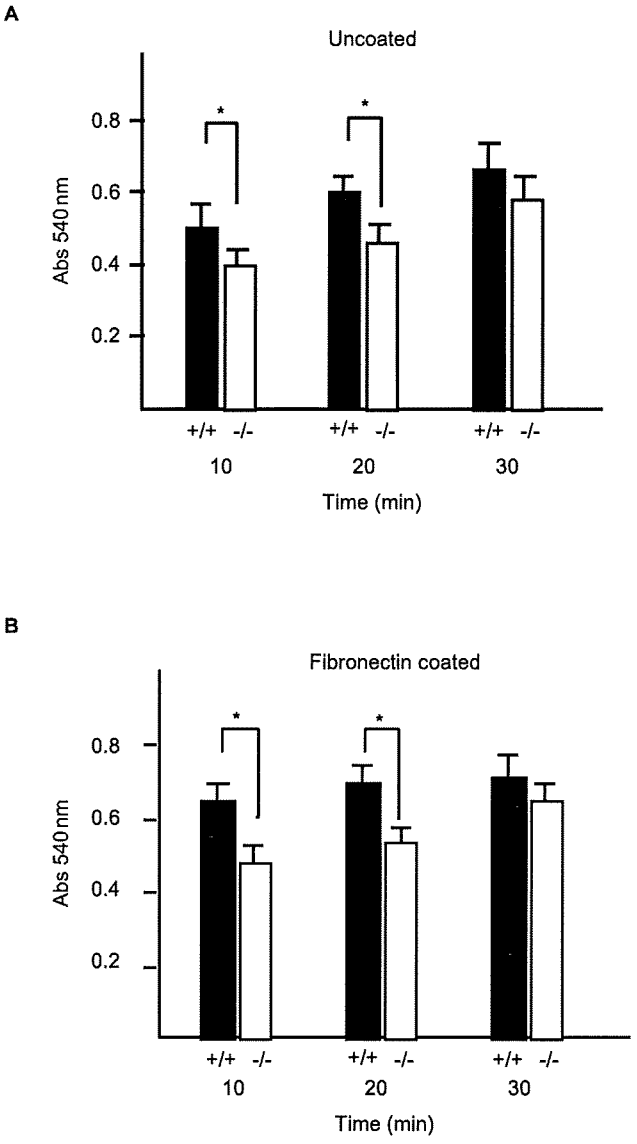

Fig. 5. **Cell adhesion of wild-type and *CatE*$^{-/-}$ macrophages on uncoated or fibronection-treated plates.** Peritoneal macrophages (5×10^5 cells) were added to uncoated or fibronectin-treated plastic wells, and subsequently incubated at 37°C for 10, 20 or 30 min. After washing, bound cells were fixed with 4% paraformaldehyde in PBS, and then stained with crystal violet. The stained plates were assayed with a microplate reader at 540 nm. The data are means ± SD for four independent experiments. *$P < 0.05$, *vs.* the corresponding values obtained with the wild-type macrophages, obtained with the unpaired Student's *t*-test.

LAMP proteins are clearly attenuated in *CatE*$^{-/-}$ macrophages, implying an abnormal membrane trafficking of some proteins in *CatE*$^{-/-}$ cells.

The abnormal membrane trafficking in *CatE*$^{-/-}$ cells is probably responsible for the accumulation of various lysosomal membrane sialoglycoproteins including LAMP-1 and LAMP-2. This is because cathepsin E deficiency induces a novel-form lysosomal storage disorder characterized by the accumulation of LAMPs (*9*). Therefore, these accumulations in endosomes and lysosomes probably influence the defects in the trafficking of membrane proteins in endocytic pathways. Similar abnormal membrane trafficking is observed in other lysosomal storage diseases such as Gaucher disease (β-glucosidase deficiency) (*27*), Pompe diseases (α-glucosidase deficiency) (*28*), neuronal ceroid lipofuscinosis (CLN3 or battenin deficiency) (*29*) and Niemann–Pick type A or B disease (sphingomyelinase deficiency) (*30*). It has been proposed that accumulation of metabolites due to lack of a lysosomal enzyme causes a certain 'traffic jam' in the endocytic pathways including those at the cell surface (*31*, *32*). Moreover, it has been reported that the treatment of cells with substances that are indigestible by lysosomes, which induces lysosomal storage-like phenotypes, and results in the accumulation of the cell-surface proteins MUC1 and CD29 cell surface proteins in endocytic vesicles (*33*). Thus, in a manner analogous to these phenotypes of storage disorders, it is likely that cathepsin E deficiency primarily causes accumulation of LAMPs; secondarily leading to the abnormal membrane trafficking of LAMPs and other receptors to the cell surface.

The molecular mechanisms in which cathepsin E deficiency impairs chemotactic responses and cell-adhesion ability remain to be determined. However, several studies have reported that chemotaxis of cells from lysosomal storage diseases are clearly reduced in comparison with that of cells from normal humans. For example, impaired chemotaxis was observed in cells from Gaucher disease (*34*) and mucolipidosis II (*35*). Given that cathepsin E deficiency leads to a lysosomal storage-like disorder in macrophages, it is possible that the lack of cathepsin E causes a defective chemotaxis similar to those lysosomal storage diseases.

In contrast to abnormal membrane trafficking to the cell-surface, endocytosis was normally processed in *CatE*$^{-/-}$ cells. Consistent with the results of this study, the phagocytosis of *S. aureus* in *CatE*$^{-/-}$ macrophages has been shown to be normal (*8*). However, compared with the wild-type cells, dendritic cells from *CatE*$^{-/-}$ mice exhibit enhanced phagocytosis and increased surface expression of the costimulatory molecules CD86, CD80 and CD40 (*18*). Although the precise mechanisms are still unknown, the discrepancy in phagocytosis and membrane trafficking between macrophages and dendritic cells from *CatE*$^{-/-}$ mice may be explained by the findings that dendritic cells have a specialized endocytic pathway, constituting specific compartments for antigen presentation such as the major histocompatibility complex II compartments and class II vesicles (*34*, *35*).

In conclusion, the present study indicates impaired chemotactic and cell-adhesion ability in *CatE*$^{-/-}$ macrophages, probably due to the decreased cell-surface levels of chemotactic and cell-adhesion receptors.

FUNDING

Nagasaki University President's Fund Grant (partial); Terumo Life Science Foundation (to T.T); Grant-in-Aid for Scientific Research from the Ministry of Education,

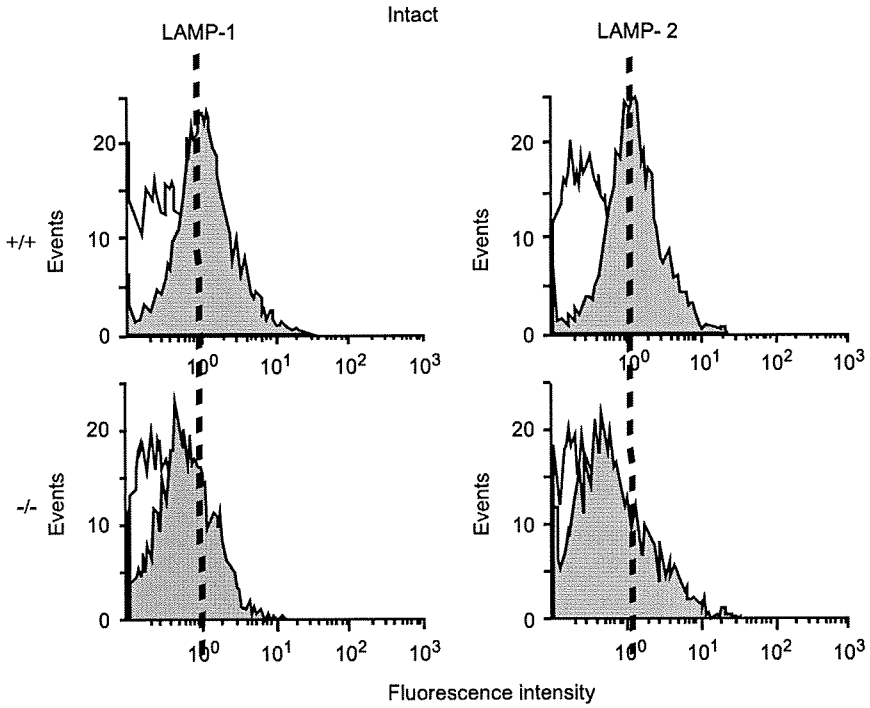

Fig. 6. **Surface expressions of LAMP-1 and LAMP-2 in wild-type or *CatE*$^{-/-}$ macrophages.** Macrophages (2×10^5 cells) from wild-type and *CatE*$^{-/-}$ mice were stained for the cell surface with specific antibodies for LAMP-1 and LAMP-2, subsequently treated with FITC-labelled second antibodies and then analysed by flow cytometry. Data are representative of five independent experiments.

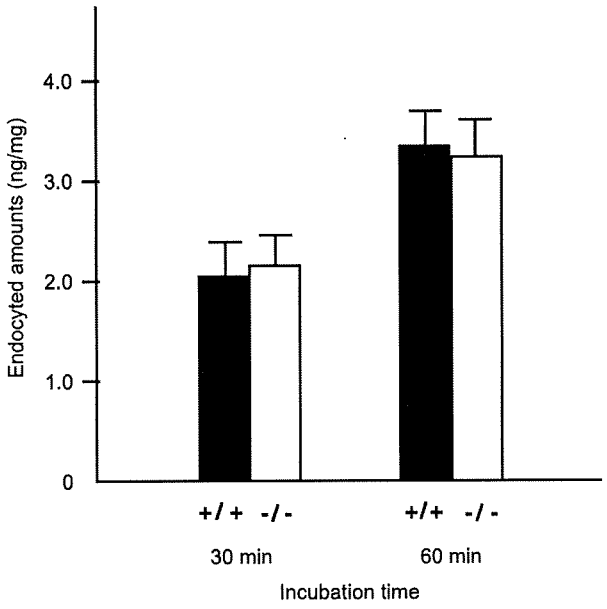

Fig. 7. **Endocytosis of FITC-dextran by wild-type or *CatE*$^{-/-}$ macrophages.** Macrophages (5×10^6 cells) were incubated with FITC-dextran (20 μg/ml) for 30 or 60 min. After washing, cells were lysed in 50 mM Tris–HCl buffer (pH 8.5) containing 0.1% Triton X-100. The amounts of fluorescence in the cell lysates were measured by spectrofluorometry and normalized to the total cell-protein concentration.

Culture, Sports, Science, and Technology of Japan (to T.T., K.Y.).

CONFLICT OF INTEREST

None declared.

REFERENCES

1. Yamamoto, K. (1999) Cathepsin E and cathepsin D in *Proteases: New Perspectives* (Turk, V., ed.) pp. 59–71, Birkhauser, Basel, Switzerland
2. Saku, T., Sakai, H., Shibata, Y., Kato, Y., and Yamamoto, K. (1991) An immunocytochemical study on distinct intracellular localization of cathepsin E and cathepsin D in human gastric cells and various rat cells. *J. Biochem.* **110**, 956–964
3. Yasuda, Y., Tsukuba, T., Okamoto, K., Kadowaki, T., and Yamamoto, K. (2005) The Role of the cathepsin E propeptide in correct folding, maturation and sorting to the endosome. *J. Biochem.* **138**, 621–630
4. Sastradipura, D.F., Nakanishi, H., Tsukuba, T., Nishishita, K., Sakai, H., Kato, Y., Gotow, T., Uchiyama, Y., and Yamamoto, K. (1998) Identification of cellular compartments involved in processing of cathepsin E in primary cultures of rat microglia. *J. Neurochem.* **70**, 2045–2056
5. Nishioku, T., Hashimoto, K., Yamashita, K., Liou, S.Y., Kagamiishi, Y., Maegawa, H., Katsube, N., Peters, C., von Figura, K., Saftig, P., Katunuma, N., Yamamoto, K., and Nakanishi, H. (2002) Involvement of cathepsin E in exogenous antigen processing in primary cultured murine microglia. *J. Biol. Chem.* **277**, 4816–4822

6. Chain, B.M., Free, P., Medd, P., Swwetman, C., Tabor, B., and Terazzini, N. (2005) The expression and function of cathepsin E in dendritic cells. *J. Immunol.* **174**, 1791–1800
7. Tsukuba, T., Okamoto, K., Okamoto, Y., Yanagawa, M., Kohmura, K., Yasuda, Y., Uchi, H., Nakahara, T., Furue, M., Nakayama, K., Kadowaki, T., Yamamoto, K., and Nakayama, K.I. (2003) Association of cathepsin E deficiency with development of atopic dermatitis. *J. Biochem.* **134**, 893–902
8. Tsukuba, T., Yamamoto, S., Yanagawa, M., Okamoto, K., Okamoto, Y., Nakayama, K.I., Kadowaki, T., and Yamamoto, K. (2006) Cathepsin E-deficient mice show increased susceptibility to bacterial infection associated with the decreased expression of multiple cell surface Toll-like receptors. *J. Biochem.* **140**, 57–66
9. Yanagawa, M., Tsukuba, T., Nishioku, T., Okamoto, Y., Okamoto, K., Takii, R., Terada, Y, Nakayama, K.I., Kadowaki, T., and Yamamoto, K. (2007) Cathepsin E deficiency induces a novel form of lysosomal storage disorder in macrophages showing the accumulation of lysosomal membrane sialoglycoproteins and the elevation of lysosomal pH. *J. Biol. Chem.* **282**, 1851–1862
10. Mellman, I., Fuchs, R., and Helenius, A. (1986) Acidification of the endocytic and exocytic pathways. *Annu. Rev. Biochem.* **55**, 663–700
11. Wu, M.M., Grabe, M., Adams, S., Tsien, R.Y., Moore, H.P., and Machen, T.E. (2001) Mechanisms of pH regulation in the regulated secretory pathway. *J. Biol. Chem.* **276**, 33027–33035
12. Weisz, O.A. (2003) Organelle acidification and disease. *Traffic* **4**, 57–64
13. Taylor, P.R., Martinez-Pomares, L., Stacey, M., Lin, H.H., Brown, G.D., and Gordon, S. (2005) Macrophage receptors and immune recognition. *Annu. Rev. Immunol.* **23**, 901–944
14. Mackay, C.R. (2001) Chemokines: immunology's high impact factors. *Nat. Immunol.* **2**, 95–101
15. Zotnik, A. and Yoshie, O. (2000) Chemokines: a new classification system and their role in immunity. *Immunity* **12**, 121–127
16. Migeotte, I., Communi, D., and Parmentier, M. (2006) Formyl peptide receptors: a promiscuous subfamily of G protein-coupled receptors controlling immune responses. *Cytokine Growth Factor Rev.* **17**, 501–519
17. Sallusto, F., Mackay, C.R., and Lanzavecchia, A. (2000) The role of chemokine receptors in primary, effector, and memory immune responses. *Annu. Rev. Immunol.* **18**, 593–620
18. Kakehashi, H., Nishioku, T., Tsukuba, T., Kadowaki, T., Nakamura, S., and Yamamoto, K. (2007) Differential regulation of the nature and functions of dendritic cells and macrophages by cathepsin E. *J. Immunol.* **179**, 5728–5737
19. Luo, B.H., Carman, C.V., and Springer, T.A. (2007) Structural basis of integrin regulation and signaling. *Annu. Rev. Immunol.* **25**, 619–647
20. Harris, E.S., Prescott, S.M., McIntyre, T.M., and Zimmerman, G.A. (2000) The leukocyte integrins. *J. Biol. Chem.* **275**, 23409–23412
21. Gahmberg, C.G. (1997) Leukocyte adhesion: CD11/CD18 integrins and intercellular adhesion molecules. *Curr. Opin. Cell Biol.* **9**, 643–650
22. Berton, G. and Lowell, C.A. (1999) Integrin signalling in neutrophils and macrophages. *Cell Signal.* **11**, 621–635
23. Luo, B.H. and Springer, T.A. (2006) Integrin structures and conformational signaling. *Curr. Opin. Cell Biol.* **18**, 579–586
24. Werthen, M., Sellborn, A., Källtorp, M., Elwing, H., and Thomsen, P. (2001) In vitro study of monocyte viability during the initial adhesion to albumin- and fibrinogen-coated surfaces. *Biomaterials.* **22**, 827–832
25. Fukuda, M. (1991) Lysosomal membrane glycoproteins. Structure, biosynthesis, and intracellular trafficking. *J. Biol. Chem.* **266**, 21327–21330
26. Eskelinen, E.L., Tanaka, Y., and Saftig, P. (2003) At the acidic edge: emerging functions for lysosomal membrane proteins. *Trends. Cell Biol.* **13**, 137–145
27. Schmitz, M., Alfalah, M., Aerts, J.M., Naim, H.Y., and Zimmer, K.P. (2005) Impaired trafficking of mutants of lysosomal glucocerebrosidase in Gaucher' s disease. *Int. J. Biochem. Cell Biol.* **37**, 2310–2320
28. Meikle, P.J., Yan, M., Ravenscroft, E.M., Isaac, E.L, Hopwood, J.J., and Brooks, D.A. (1999) Altered trafficking and turnover of LAMP-1 in Pompe disease-affected cells. *Mol. Genet. Metab.* **66**, 179–188
29. Fossale, E., Wolf, P., Espinola, J.A., Lubicz-Nawrocka, T., Teed, A.M., Gao, H., Rigamonti, D., Cattaneo, E., MacDonald, M.E., and Cotman, S.L. (2004) Membrane trafficking and mitochondrial abnormalities precede subunit c deposition in a cerebellar cell model of juvenile neuronal ceroid lipofuscinosis. *BMC Neurosci.* **5**, 57
30. Pagano, R.E., Puri, V., Dominguez, M., and Marks, D.L. (2000) Membrane traffic in sphingolipid storage diseases. *Traffic* **1**, 807–815
31. Simons, K. and Gruenberg, J. (2000) Jamming the endosomal system: lipid rafts and lysosomal storage diseases. *Trends Cell Biol.* **10**, 459–462
32. Futerman, A.H. and van Meer, G. (2004) The cell biology of lysosomal storage disorders. *Nat. Rev. Mol. Cell Biol.* **5**, 554–565
33. Ulloa, F. and Real, F.X. (2003) Benzyl-*N*-acetyl-alpha-D-galactosaminide induces a storage disease-like phenotype by perturbing the endocytic pathway. *J. Biol. Chem.* **278**, 12374–12383
34. Aker, M., Zimran, A., Abrahamov, A., Horowitz, M., and Matzner, Y. (1993) Abnormal neutrophil chemotaxis in Gaucher disease. *Brit. J. Haematol.* **83**, 187–191
35. Sakaguchi, T., Kikuchi, K., Ito, S., and Mikawa, H. (1988) Impaired neutrophil chemotaxis in two patients with mucolipidosis II. *Act. Paediatr. Scand.* **77**, 608–609

Laboratory Investigation (2009), 1–12

Human synovial sarcoma proto-oncogene Syt is essential for early embryonic development through the regulation of cell migration

Taichi Kimura[1], Mieko Sakai[1], Kouichi Tabu[1], Lei Wang[1], Ryosuke Tsunematsu[2], Masumi Tsuda[3], Hirofumi Sawa[1,*], Kazuo Nagashima[1,†], Hiroshi Nishihara[1], Shigetsugu Hatakeyama[4], Keiko Nakayama[5], Marc Ladanyi[6], Shinya Tanaka[1] and Keiichi I Nakayama[2]

SYT–SSX protein, resulted from chromosomal translocation, causes synovial sarcoma, which is a malignant tumor accounting for 10% of soft tissue sarcoma. However, biological functions of SYT (synovial sarcoma translocation), also known as SS18, are largely unclear, whereas it has been proven that *Syt*-null mice die at early stages of embryonic development. Here, we generated *Syt*-deficient mice and confirmed the reported phenotypes, including growth retardation, open neural tube and haplo-insufficient lethality, and therefore, there is no doubt that Syt is essential for embryonic development. However, placental defects, described in the earlier report, were rarely seen in our mice and we frequently observed cardiac defect in *Syt*-deficient mice. As the mechanisms responsible for embryonic lethality seem to be complicate, we performed additional experiments. By using primary cultured embryonic fibroblasts, we showed that $Syt^{-/-}$ MEFs deregulate actin organization and suppressed cell migration. These observations suggest that Syt may contribute to the signaling pathway important for various cellular functions *in vivo* and *in vitro*, and we propose that *Syt*-deficient MEFs would be a powerful means to understand the biological roles of SYT *in vitro*.
Laboratory Investigation advance online publication, 30 March 2009; doi:10.1038/labinvest.2009.25

KEYWORDS: Syt; p300; synovial sarcoma; embryonic lethality; cardiogenesis; motility

Human synovial sarcoma is an aggressive tumor that accounts for almost 10% of all soft tissue sarcomas and typically arises in the para-articular regions in young adults.[1,2] Synovial sarcoma possesses a specific chromosomal translocation between chromosomes (chr) 18 and X, forming a chimeric gene fusing SYT (synovial sarcoma translocation) on chr 18 to SSX (synovial sarcoma X break point) on chr X.[3] The translocation found in synovial sarcoma removes the last eight amino acids of SYT and fuses it to the C-terminal portion of the SSX to yield a SYT–SSX fusion protein.[3] In contrast to SSX, which is thought to act as a transcriptional regulator because of its sequence homology to other transcription repressors, SYT does not share a homologous region or conserved domain with other human proteins.[4]

SYT is a ubiquitously expressed nuclear protein containing two distinct domains. One is the SYT amino N-terminal homology domain, which shows homology to the predicted proteins of EST clones derived from a wide variety of species, and the other is the carboxy C-terminal QPGY domain, which is rich in glutamine, proline, glycine and tyrosine.[5] The QPGY domain was shown to activate the transcription of a reporter gene when it was fused to a DNA-binding domain.[5,6] As SYT lacks a DNA-binding domain, it may function as a transcriptional co-activator.[6] In fact, SYT has been shown to

[1]Laboratory of Molecular and Cellular Pathology, Graduate School of Medicine, Hokkaido University, Sapporo, Japan; [2]Department of Molecular and Cellular Biology, Medical Institute of Bioregulation, Kyushu University, Fukuoka, Fukuoka, Japan; [3]Department of Laboratory Medicine, Hokkaido University Graduate School of Medicine, Sapporo, Japan; [4]Department of Molecular Biochemistry, Hokkaido University Graduate School of Medicine, Sapporo, Japan; [5]Department of Developmental Biology, Center for Translational and Advanced Animal Research on Human Disease, Graduate School of Medicine, Tohoku University, Aobaku, Sendai, Japan and [6]Department of Pathology, Memorial Sloan-Kettering Cancer Center, New York, NY, USA
Correspondence: Professor S Tanaka, MD, PhD, Laboratory of Molecular and Cellular Pathology, Hokkaido University School of Medicine, N 15, W 7, Kita-ku, Sapporo 060-8638, Japan.
E-mail: tanaka@med.hokudai.ac.jp
*Current address: Hirofumi Sawa, Department of Pathobiology, Hokkaido University Zoonosis Research Center, and 21st Century COE Program for Zoonosis Control, N12, W9, Sapporo, Japan
†Current address: Kazuo Nagashima, Sapporo Higashi Tokushukai Hospital, N33, E13, Sapporo, Japan
Received 25 January 2009; revised 22 February 2009; accepted 27 February 2009; published online 30 March 2009

bind to hBRM/hSNF2α, a major component of the SWI/SNF-type chromatin remodeling complex.[5,7–9] Moreover, it was also shown that SYT interacts with the putative transcriptional factor AF10, histone acetyl transferase p300 and a component of histone deacetylase complex mSin3A.[10–12] Thus, it is possible that SYT regulates transcription through the binding to chromatin modifiers. In spite of these biochemical studies of SYT, the physiological function of SYT remains largely unknown.

To examine the role of SYT *in vivo*, we established *Syt*-deficient mice by a gene targeting strategy. $Syt^{-/-}$ homozygous mutant mice died around mid-gestation and exhibited multiple defects in morphogenesis. These results support the essential gene dosage-sensitive role of Syt in embryogenesis. Subsequently, to examine cellular basis of these phenotypes, we established MEFs from wild-type and $Syt^{-/-}$ at E9.75. We found that the absence of Syt affects cell migration. These results suggest that SYT plays an important role in cellular motility through the regulation of cytoskeletal organization.

MATERIALS AND METHODS

Generation of Syt Knockout Mice

A targeting vector, designed to delete exons 1 and 2 of the Syt gene, was constructed using a PKG-lox-Neo-poly(A) cassette as described earlier.[13] Briefly, the targeted embryonic stem cell clone was microinjected into host blastocysts, and the resulting chimeric mice were C57BL/6 mice to achieve germ-line transmission of the *Syt* mutation. The mice used in this study were of mixed genetic background (129/Sv and C57BL/6).

Genotyping of Mice

Genomic DNA samples (15 μg) isolated from 3-week-old mice were digested with *Eco*RV and *Spe*I and analyzed by Southern blotting. A probe for Southern blotting was generated by genomic PCR. Primer sequences used in this experiment included 5′-TTACAGAGGATTGGGAAAGG-3′ and 5′-CTGGTATTTCGCTAAGGAAG-3′. Routine genotyping of mice was performed by PCR using three primers: F 5′-GAG TCC TGC CTG GGA TGA GAA C-3′, R 5′-CGA TAG AAG ATG AAG ACT CTG GCC -3′ and PJL 5′-TGC TAA AGC GCA TGC TCC AGA CTG T-3′, which resulted in 453-bp (F/R) and 370-bp (F/PJL) products from wild-type and targeted alleles, respectively.

Histopathological and Immunohistochemical Analysis

Embryos were fixed with 4% paraformaldehyde in phosphate-buffered saline and embedded in paraffin. Four-μm tissue sections were deparaffinized with xylene and rehydrated through a graded ethanol series and subjected to hematoxylin and eosin stain. Histopathological examination was performed by trained histopathologists. For immunohistochemical analysis, antigens were retrieved in citrate buffer (pH 6.0) by using a pressure cooker. Then, sections were incubated with 0.3% H_2O_2 in methanol to quench endogenous peroxidase activity and then treated with normal rabbit or goat serum to eliminate nonspecific binding of the antibodies. After treatment, sections were incubated with primary antibodies for PCNA (M879; DakoCytomation, CA, USA), hBRM (a gift from Yasunori Machida in Nagoya University, Japan), BRG1 (a gift from Yasunori Machida in Nagoya University, Japan) and mSYT (generated in our lab) at 4°C overnight. After incubation with the biotinylated secondary antibody, immunoreaction products were visualized with enzymatic reaction of peroxidase, with 3, 3′-diaminobenzidine tetrahydrochloride (DAB) as a substrate.

Terminal Deoxynucleotidyltransferase-Mediated dUTP-Biotin Nick End Labeling Assay

Paraffin-embedded tissue sections were deparaffinized and washed with 0.1 M phosphate buffer for a few minutes, and permeabilized for 20 min at room temperature (RT) with proteinase K (20 μg/ml in 0.1 M phosphate buffer) and bleached with 2% H_2O_2 for 7 min at RT. Thereafter, the samples were washed with terminal deoxynucleotidyl transferase (TdT) buffer composed of 30 mM Tris-HCl (pH 7.2), 140 mM sodium cacodylate and 1 mM cobalt chloride, and incubated for 90 min at RT with TdT reaction mixture containing TdT and biotinylated dUTP in TdT buffer. Labeled DNA was visualized with enzymatic reaction of peroxidase and DAB.

Electron Microscopic Analysis

Embryos were fixed with 2.5% glutaraldehyde (TAAB; Laboratory Equipment, Aldermaston, UK) in 0.1 M phosphate buffer at 4°C for 40 h, and then washed with 7% sucrose in 0.1 M phosphate buffer. Thereafter, the samples were fixed with 1% OsO_4 (Next Chimica, South Africa) in 0.1 M phosphate buffer at RT for 90 min and gradually dehydrated with 50, 70 and 95% acetone in ethanol for 15 min each; 95% acetone for 15 min; and 100% acetone three times for 20 min each. Afterward, the samples were treated with epon solution containing 60% solution A (a mixture of 62 ml of epon 812 (TAAB) and 100 ml of dodecenyl succinic anhydride) and 40% solution B (a mixture of 100 ml of epon 812 and 89 ml of methyl nadic anhydride). The samples were treated with epon/acetone (1:1) overnight, epon/acetone (3:1) for 1 h and epon solution for 1 h, and embedded in epon with 1.5% 2, 4, 6-tri(dimethylaminomethyl)phenol in a capsule (Nissin EM, Tokyo, Japan). The embedded samples were sectioned on an ultramicrotome at 0.1-μm thickness, put onto a grid (TAAB) and treated with 1.5% uranyl acetate (Merk, Darmstadt, Germany) for 20 min and 0.2% lead citrate (Kishida Chemistry, Tokyo, Japan) for 15 min. Finally, the samples were observed with an electron microscope (Hitachi 7100, Tokyo, Japan).

Immunoblot Analysis

Immunoblotting was performed according to a standard protocol described elsewhere.[14] Briefly, embryos were lysed with lysis buffer composed of 50 mM Tris-HCl (pH 7.6), 150 mM NaCl, 0.5% Triton X-100, 1 mM PMSF and 1 mM Na_3VO_4, and clarified by microcentrifugation at 12 000 *g* for 10 min at 4°C. Supernatants containing 20 μg of proteins were subjected to SDS-PAGE, and separated proteins were transferred to PVDF filters. The filters were blocked with 5% skim milk and incubated with primary antibodies for hBRM, BRG1, p300 (N-15; Santa Cruz Biotechnology, CA, USA), mSYT and α-tubulin (B-5-1-2; Sigma, MI, USA). Antibody binding was visualized by chemiluminescence (ELC; Amersham Pharmacia Biotech, NJ, USA).

RNA Extraction, Labeling and Hybridization

For microarray analysis, RNA was isolated from embryos or MEFs using the RNeasy mini kit (Qiagen, CA, USA). For microarray studies, labeling and hybridization were performed according to Affymetrix standard protocols. Labeled cRNA was hybridized onto the Affymetrix GeneChip Mouse Genome 430A 2.0 array (Affymetrix, CA, USA), which contains 22 691 probes. Microarray slides were scanned using the Affymetrix GCS 2500 scanner to collect fluorescence signal.

Preparation of MEFs and Cell Cultures

Primary MEFs were obtained from 9.75 d.p.c. embryos that were either wild-type or $Syt^{-/-}$ using established procedure.[15] Cells were cultured at 37°C (6% CO_2) in MEF medium (Dulbecco's modified Eagle's medium containing 10% fetal bovine serum supplemented with 2 mM L-glutamine, 0.1 mM sodium pyruvate, 0.1 mM MEM nonessential amino-acid solution, 100 U/ml penicillin G, 100 μg/ml streptomycin and 50 μM 2-mercaptoethanol).

Immunocytofluorescence and Confocal Microscopy

Wild-type and $Syt^{-/-}$ MEFs were grown on Lab-Tek chamber slides (Nalge Nunc, NY, USA) in MEF medium, were fixed with 3% paraformaldehyde in PBS for 15 min, permeabilized with 0.5% Triton X-100 in PBS for 5 min and incubated with 1% bovine serum albumin in PBS for 20 min at RT. They were then incubated overnight at 4°C with mouse monoclonal antibodies specific for paxillin (1:2000; BD Transduction Laboratories, CA, USA), then for 1 h at RT with Alexa Fluor 488-conjugated secondary antibodies (Molecular Probes, OR, USA) and finally for 30 min at RT with Alexa Fluor 594-conjugated phalloidin (Molecular Probes). The cells were then examined with a confocal laser-scanning microscope equipped with a computer (MRC-1024; Bio-Rad Microscience, CA, USA).

Wound Closure Assay

The wound closure assay was performed as described.[16] Wild-type and $Syt^{-/-}$ MEFs were grown in MEF medium for 48 h. The confluent cells were wounded by scratching the monolayer with a pipette tip, washed twice with PBS, allowed to migrate in MEF medium for the indicated times and photographed. The assay was performed in triplicate.

Semi-Quantitative Reverse Transcription PCR Analysis

Total RNA was isolated from wild-type and $Syt^{-/-}$ MEFs using RNeasy mini kit (Qiagen) according to the manufacturer's instruction. Reverse transcription was carried out with Superscript II RT (Invitrogen, CA, USA) according to the manufacturer's instruction. One hundred nanograms of the resulting first-strand cDNA was used as template and amplified by PCR using KOD-Plus DNA polymerase (Toyobo, Osaka, Japan). Sequences of the oligonucleotide primer sets used for reverse transcription PCR (RT-PCR) analysis are as follows: CD44: forward 5′-GCA CCC CAG AAG GCT ACA TTT-3′, reverse 5′-TCT GCC CAC ACC TTC TCC TAC TAT-3′; FoxG1: forward 5′-CAG CAC TTT GAG TTA CAA CG-3′, reverse 5′-TGG TCT GCG AAG TCA TTG AC-3′; HMGA2: forward 5′-AAC CTT ACT GGG TCG GCA TC-3′, reverse 5′-GGT GAG GTT TGA GCT CCT TC-3′; IGFR2: forward 5′-CAG GTA GCG AAA AGT GGT AAG T-3′, reverse 5′-GCC TGG TCT GTT TCT GTG ATT G-3′; Neuropilin: forward 5′-GAA TGT TGG GCA TGG TGT CT-3′; reverse 5′-CTT AGCCTTGCGCTTGCT-3′; Neurotrophin3: forward 5′-AAA ACC GGT AAC TCT CCT GTG-3′, reverse 5′-CTA CGA GTT TGT TGT TTT CTG-3′, PDGFRB: forward 5′-AGG TCA TTG AGT CTG TGA GC-3′, reverse 5′-ATC GGC AGT ATT CCG TGA TG-3′; Pleiotrophin: forward 5′-ACT GGC GCC GAG TGC AAACAG-3′, reverse 5′-GAG CTT GCC ACA GGG CTT GGA-3′; RGEF4: forward 5′-GCC TAT TCG TGG CTC TG-3′, reverse 5′-CAGACCTCAGTGACAACC-3′; RUNX2: forward 5′-CTC TGG CCT TCC TCT CTC AGT AA-3′, reverse 5′-TAG GTA AAG GTG GCT GGG TAG TG-3′; SDF1: forward 5′-ACT TTC CCT CTC GGT CCA C-3′, reverse 5′-TTG TTT AAA GCT TTC TCC AGG TA-3′; TCF-4: forward 5′-GGG GCT CAT ACT CAT CTT-3′, reverse 5′-GCC TGT CCT CCA TTT CTA-3′; GAPDH: forward 5′-GTC GTG GAG TCT ACT GGT GTC-3′, reverse 5′-GAG CCC TTC CAC AAT GCC AAA-3′.

RESULTS

Generation of Syt-Deficient Mice

A targeting vector containing a Neo cassette was used to replace the 5.2-kb genomic sequence of *Syt* gene including exon 1and exon 2 through homologous recombination (Figure 1a). Southern blot analysis using tail DNA from 3-week-old mice confirmed that Syt $^{+/-}$ mouse carried targeted allele (Figure 1b). Targeting of the *Syt* gene was also confirmed by immunohistochemistry and immunoblotting using E10.5 mouse embryos (Figure 1c and d). Heterozygous embryos seemed to express less amount of Syt protein than wild-type embryos (Figure 1d).

To date, none of the $Syt^{-/-}$ homozygous mutant has been detected among the 202 newborns from heterozygote crosses. $Syt^{+/-}$ heterozygous offspring appeared to be normal and

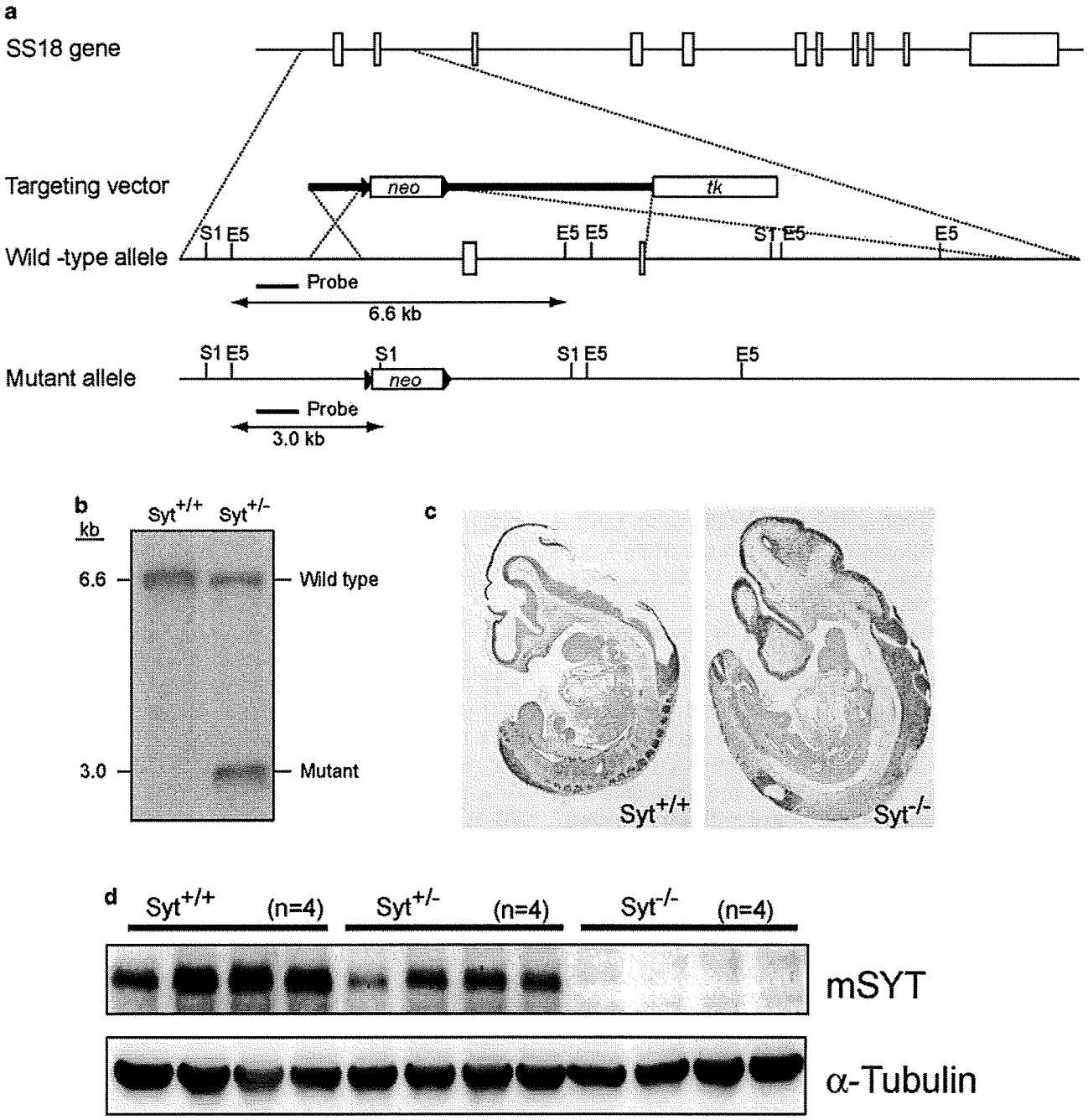

Figure 1 Targeting disruption of the Syt locus and the establishment of a mutant mouse strain. (**a**) Schematic representation of the wild-type allele, targeting vector and targeted allele. The open boxes on the alleles represent the exons. A Neo cassette replaced exons 1 and 2 of the *Syt* gene. The expected sizes of the *Eco*RV (E5) and *Spe*I (S1) digestion products of the gene, hybridized with the indicated probe, are shown. (**b**) Genomic DNA isolated from 3-week-old mice was digested with *Eco*RV and *Spe*I, and analyzed by Southern blotting with the probe shown in (**a**). (**c**) Wild-type (left) and homozygous (right) E10.5 embryos were subjected to immunohistochemistry using an anti-mSYT antibody. (**d**) Protein extracts (30 μg) from wild-type (lanes 1–4), heterozygous (lanes 5–8) and homozygous E10.5 embryos (lanes 9–12) were analyzed by immunoblotting using an anti-mSYT antibody.

fertile. The rate of $Syt^{+/-}$ heterozygous mutants among newborns was 38% lower than that expected by Mendelian inheritance (Table 1). As no neonatal lethality was observed, a certain population of $Syt^{+/-}$ heterozygous embryos must have died very early *in utero*.

Histopathological Examination of Syt-Deficient Mice

To determine the time point at which the $Syt^{-/-}$ mutant embryos become lethal, we examined embryos from $Syt^{+/-}$ intercrosses at various developmental stages. Most of $Syt^{-/-}$ homozygous embryos were alive at E9.5. At E10.5, approxi-

Table 1 Genotype of embryos from Syt heterozygous intercrosses

Embryonic day	Numbers of analyzed mice			
	+/+	+/−	−/− (abnormal[a])	Total
E7.5	8	4	5 (0)	17
E8.5	6	8	5 (0)	27
E9.5	202	411	190 (30)	803
E10.5	118	229	105 (51)	452
E11.5	25	60	21 (17)	106
E13.5	12	16	1 (1)	29
New born	90	112	0 (0)	202

[a]The number of embryos with a macroscopic abnormality is indicated in parentheses.

mately 50% of $Syt^{-/-}$ embryos were already dead as judged by heartbeats or the signs of re-absorption, and no $Syt^{-/-}$ homozygous mutants could be retrieved after E11.5 (Table 1). The $Syt^{-/-}$ embryos dissected at E9.75 were developmentally retarded in size (Figure 2a and b). The most severely affected but still viable mutant embryos usually displayed little or no signs of embryonic turning and exhibited only 10–14 somites (Figure 2c). We determined that the developmental arrest of $Syt^{-/-}$ embryos began at E8.5–E9.0, because generally, embryonic turning starts at E8.5 (8 somites) and is completed around E9.0 (16 somites).

Morphologically, all $Syt^{-/-}$ embryos could be distinguished from their wild-type littermates as early as E9.5 by their severe open neural tube as the neural tube begins to close at E8.5 and is completed by E9.0. These also suggest that developmental arrest of $Syt^{-/-}$ embryos was caused at E8.5–E9.0. In addition, various degrees of exencephaly were observed in $Syt^{-/-}$ embryos. Typically, the neural tube failed to fuse at the hindbrain and forebrain (Figure 2b and c). In the most severely affected mutants (data not shown), it remained completely open. Histological examination of E10.5 embryos revealed the exencephaly was caused by failure of neural tube closure (compare Figure 2d and e). The heterogeneity in the severity of Syt mutants indicates a partial penetration of the phenotypes possibly due to the genetic modifiers.

To identify the downregulated genes that are related to the phenotypes of $Syt^{-/-}$ mutants, we performed Gene Chip analysis using wild-type and $Syt^{-/-}$ embryos at E9.75. Many genes related to embryonic growth or neuronal development were downregulated in $Syt^{-/-}$ mutants (Supplementary Table 1).

As neural tube defects generally do not cause early embryonic lethality, we examined other developmental abnormalities in $Syt^{-/-}$ mutant embryos. While this study was in progress, another group reported the establishment of *Syt*-deficient mice,[17] exhibiting embryonic lethality between E8.5 and E9.5 either through an incomplete chorio-allantoic fusion or through a defect in the subsequent process of vascular branching morphogenesis.[17]

In contrast to the above-mentioned $Syt^{-/-}$ mice, almost all of our $Syt^{-/-}$ mutant embryos displayed normal chorio-allantoic fusion and exhibited normal labyrinth formation consisting of placental and embryonic vasculature at E9.75 (Figure 2f–k), even though their developmental stages were somewhat retarded. Thus, the embryonic lethality may not be due to the placental defect in our $Syt^{-/-}$ mutant embryos.

As placental defects did not provoke early embryonic lethality, at least before E9.5, we extensively examined other developmental abnormalities in our $Syt^{-/-}$ mutant embryos. At E9.5–E10.5, a number of $Syt^{-/-}$ mutants showed an enlarged cardiac cavity. Furthermore, $Syt^{-/-}$ mutants displayed severe pericardial effusions (Figure 2c), one of the clear signs of cardiac dysfunction. Cardiac ventricular movements appeared to be weaker and less expansive in mutants compared with that in wild-type embryos. Although no overt patterning defect was observed, the ventricular chambers of mutant embryos exhibited significantly thin wall and retarded maturation of trabeculation (Figures 2l–o, 4a and b).

Immunohistochemical Analysis of Syt-Deficient Mice

As the cardiac defect was found in $Syt^{-/-}$ embryos, we examined Gene Chip data of whole embryos focusing on cardiogenesis-specific genes. However, an obvious downregulation of cardiogenesis-specific genes was not observed in $Syt^{-/-}$ mutants (Supplementary Table 2).

Therefore, for better understanding the basis for the cardiac abnormality in the $Syt^{-/-}$ mutants, we analyzed whether cardiomyocytes undergo apoptosis by terminal deoxynucleotidyltransferase-mediated dUTP-biotin nick end labeling assay. In both wild-type and $Syt^{-/-}$ embryos, no significant induction of apoptosis was observed in various tissues (Figure 3a–d). Cell growth rates were also analyzed by immunostaining using antibodies for proliferation marker proteins, such as Ki-67 antigen and PCNA. The labeling indices of Ki-67 in the neural tube of wild-type embryos were higher than those in $Syt^{-/-}$ embryos at E10.5 (Figure 3e–h). In addition, immunostaining for PCNA showed that the growth rates of cardiomyocytes in $Syt^{-/-}$ embryos were much lower than those in wild-type embryos (Figure 3i–l). These results suggest that decreased cell growth may contribute to the impaired formation of cardiac ventricle in $Syt^{-/-}$ embryos.

Ultrastructural Analysis of the Heart in $Syt^{-/-}$ Embryos

For further analysis, we employed electron microscopy. First, we carefully prepared specimens from comparable areas of the ventricular free wall in both wild-type and $Syt^{-/-}$ embryos (Figure 4a and b). After, we confirmed the abnormality of the ventricular walls by toluidine blue staining, then the corresponding areas were subjected to electron microscopy. In cardiomyocytes of $Syt^{-/-}$ embryos at E10.5, the numbers

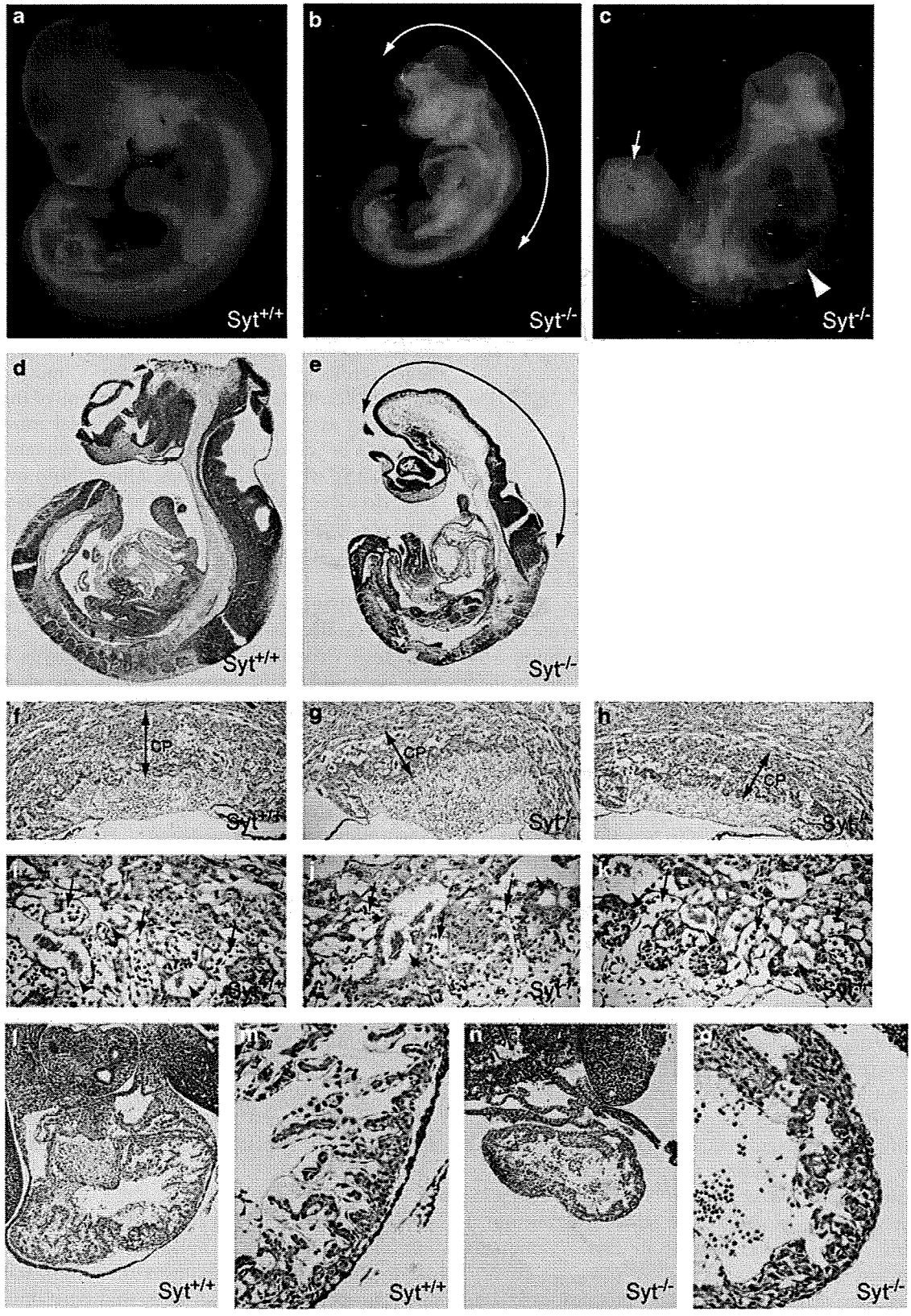
a
Syt+/+
b
Syt-/-
c
Syt-/-
d
Syt+/+
e
Syt-/-
f
CP
Syt+/+
g
CP
Syt-/-
h
CP
Syt-/-
i
Syt+/+
j
Syt-/-
k
Syt-/-
l
Syt+/+
m
Syt+/+
n
Syt-/-
o
Syt-/-

of perinuclear myofibrils and also of myofibrillar bundles were decreased (Figure 4c and d). Sarcomeric structure showed no significant difference between wild-type and $Syt^{-/-}$ mutant embryos (Figure 4e and f). Thus, cardiac development was perturbed in $Syt^{-/-}$ embryos, and this may be responsible for embryonic lethality.

Downregulation of p300 Expression in Syt-Deficient Mice

All $Syt^{-/-}$ homozygous mutants displayed lethality by E11.5, and among published gene knockout mice, especially those targeting chromatin modifiers, the phenotypes of $Syt^{-/-}$ mutants closely resembled those of p300-deficient mice.[18]

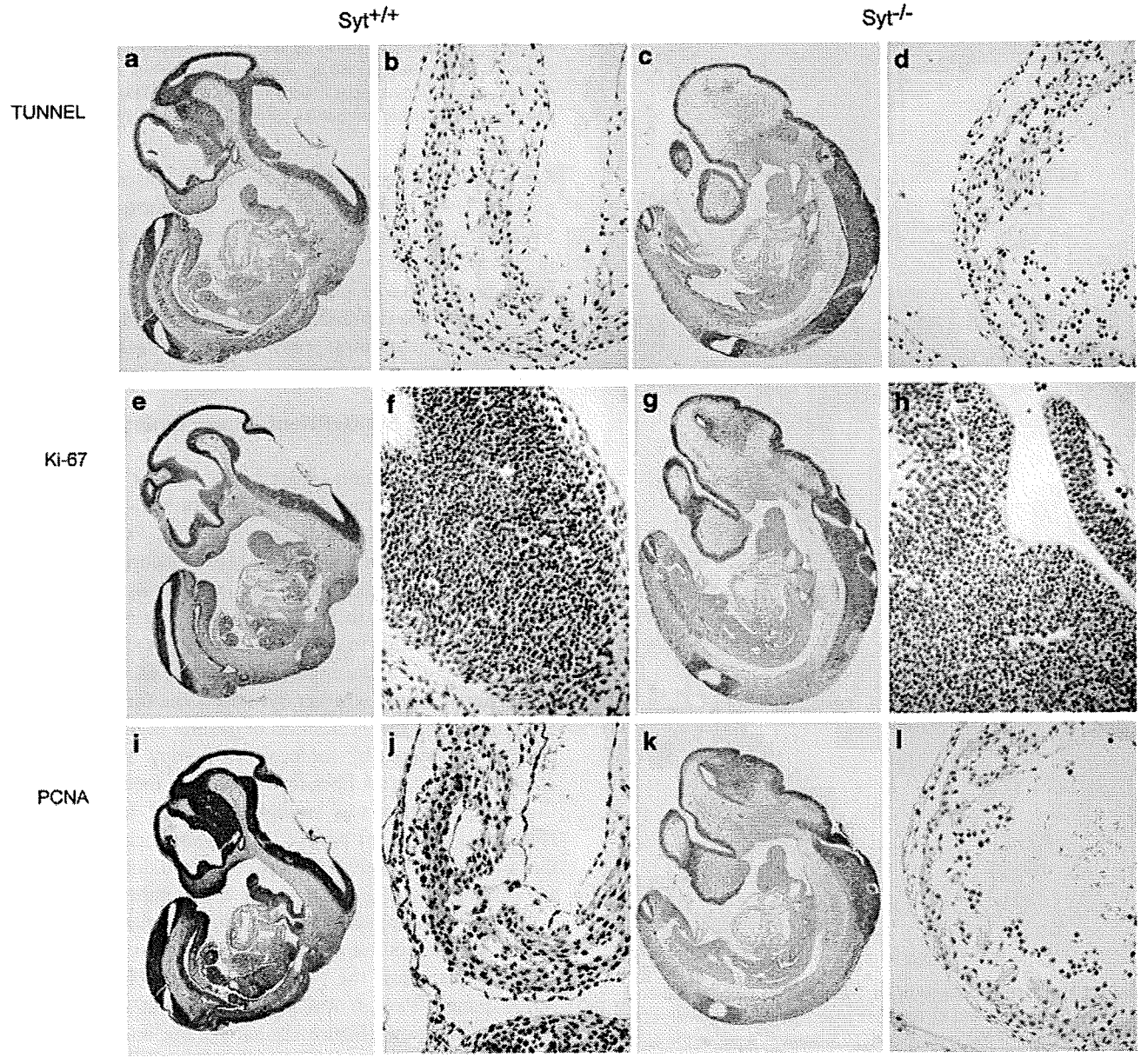

Figure 3 Immunohistochemical analysis for apoptosis and cell growth. (**a–d**) TUNEL staining; (**e–h**) immunostain for Ki-67 and (**i–l**) PCNA. $Syt^{+/+}$ (**a**, **b**, **e**, **f**, **i** and **j**) and $Syt^{+/-}$ (**c**, **d**, **g**, **h**, **k** and **l**) are indicated. Magnification ×20 (**a**, **c**, **e**, **g**, **i** and **k**) and ×400 (**b**, **d**, **f**, **h**, **j** and **l**).

Figure 2 Morphological analyses of Syt homozygous mutant embryos. (**a–c**) Representative stereoscopical appearance of embryos at E9.75 Syt+/+ (**a**) and $Syt^{-/-}$ (**b** and **c**). Double-headed arrow in panel b indicates open neural tube. Arrowheads in panel c indicate pericardial edema and arrow in panel c indicates allantois. (**d–o**) Microscopic analysis by H&E stain. Sagittal section of Syt+/+ (**d**) and $Syt^{-/-}$ (**e**) embryos at E10.5. Double-headed arrow in panel e indicates open neural tube. (**f–k**) Histopathology of $Syt^{+/+}$ (**f** and **i**) and $Syt^{-/-}$ (**g**, **h**, **j** and **k**) developing placenta at E9.75 (**i**, **j** and **k**, higher magnification of **f**, **g** and **h**, respectively). Double-headed arrows and CP in panels f–h indicate chorionic plate. Arrows in panels i–k indicate embryonic blood vessels, and arrowheads in panels i–k indicate maternal blood vessels, respectively. (**l–o**) Histopathology of Syt+/+ (**l** and **m**) and $Syt^{-/-}$ (**n** and **o**) embryonic heart at E10.5 (**m**, transverse section and **o**, higher magnification of **l** and **n**, respectively).

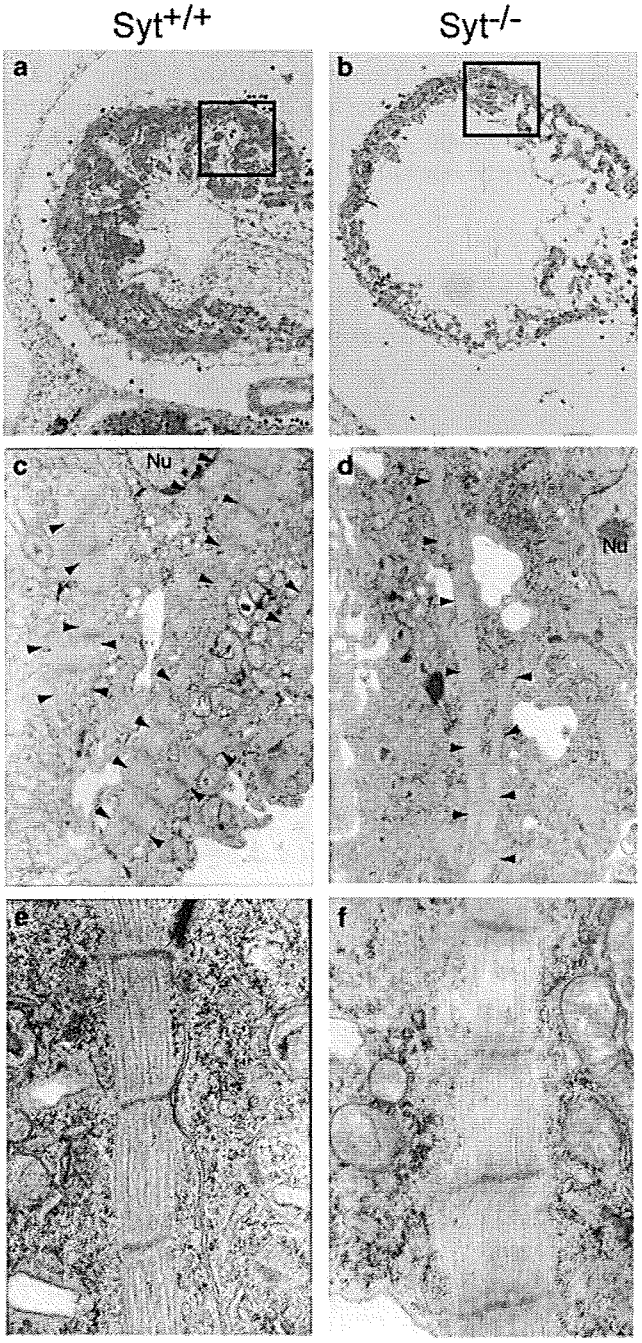

Figure 4 Ultrastructural analysis of embryonic hearts by transmission electron microscopy. (**a** and **b**) Toluidine blue stain for horizontal section of $Syt^{+/+}$ (**a**) and $Syt^{-/-}$ (**b**) embryos at E10.5. Squares indicate the areas subjected to EM analysis. (**c–f**) EM analysis of Syt+/+ (**a**, **c** and **e**) and $Syt^{-/-}$ (**b**, **d** and **f**) mutants with magnification ×5000 (**c** and **d**) and ×100 000 (**e** and **f**). Arrowheads in (**c**) and (**d**) indicate myofibrils. Nu, nuclei.

We, therefore, analyzed the expression levels of Syt-interacting proteins in $Syt^{-/-}$ embryos, focusing in particular on p300. We performed immunoblot analysis by using lysate of whole embryos of four individual lines of stage-matched $Syt^{+/+}$, $Syt^{+/-}$ and $Syt^{-/-}$ mutants, and found that the expression levels of p300 were significantly decreased in

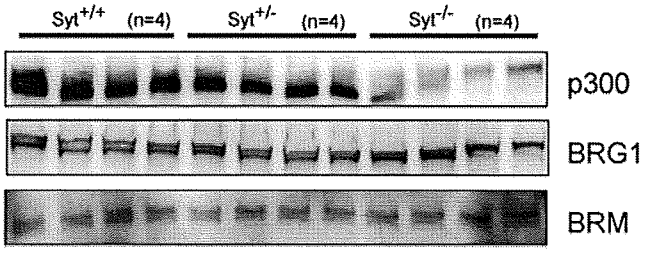

Figure 5 Immunoblot analysis of SYT-interacting proteins in $Syt^{-/-}$ embryos. Protein extracts (30 μg) from wild-type (lanes 1–4), heterozygous (lanes 5–8) and homozygous E10.5 embryos (lanes 9–12) were analyzed by immunoblotting using antibodies for p300, BRG1 and BRM.

$Syt^{-/-}$ homozygous mutants (Figure 5). In contrast, the expression levels of BRG1 and hBRM, which are components of SWI/SNF-type chromatin remodeling factors, were not significantly altered between the wild-type and Syt mutant embryos at E10.5 (Figure 5). These results suggest that Syt may regulate the expression level of p300, and the phenotype of the $Syt^{-/-}$ mutants may reflect at least in part the downregulation of p300.

Phenotypes of Syt-Deficient Mouse Embryonic Fibroblasts

To analyse the function of Syt in the cellular level, we established mouse embryonic fibroblasts from wild-type and $Syt^{-/-}$ embryos at E9.75. Interestingly, $Syt^{-/-}$ MEFs were morphologically different from wild-type MEFs (Figure 6a). Wild-type MEFs showed spindle shape, but in contrast, small rounded cells were dominant in $Syt^{-/-}$ MEFs (Figure 6a, left and right panels). In addition, in confluent culture, $Syt^{-/-}$ MEFs showed sheet cobble stone-like appearance (Figure 6a, center panel).

We next assessed whether Syt affects the formation of actin stress fibers and the localization of paxillin (a major constituent of focal adhesions) by confocal microscopy. Wild-type MEFs exhibited actin stress fiber formation and membrane ruffling; thus cell direction was readily recognized by leading edge (Figure 6b, upper left panel). In addition, localization of paxillin was diffusely observed in the cytoplasm dominantly seen at the ruffling side (Figure 6b, upper center panel).

In contrast, in small round cells, the dominant population in $Syt^{-/-}$ MEFs does not exhibit fine actin fibers but has a dense actin bundle below the plasma membrane (Figure 6b, lower center panel). Paxillin was localized only at the edge of the plasma membrane (Figure 6b, left panel), and we could not recognize directional morphology because of the loss of leading edge. For cell motility assessed by wound closure assay, after 17 h, wild-type MEFs covered most of the wounded area, but $Syt^{-/-}$ MEFs achieved only 35% (Figure 6c). Thus, Syt plays an important role in the motility of MEFs.

Expression of SYT-Interacting Proteins and Downregulated Gene Expression Profile in $Syt^{-/-}$ MEFs

To examine the molecular mechanisms of these phenotypes, we analyzed expression levels of Syt-interacting proteins in

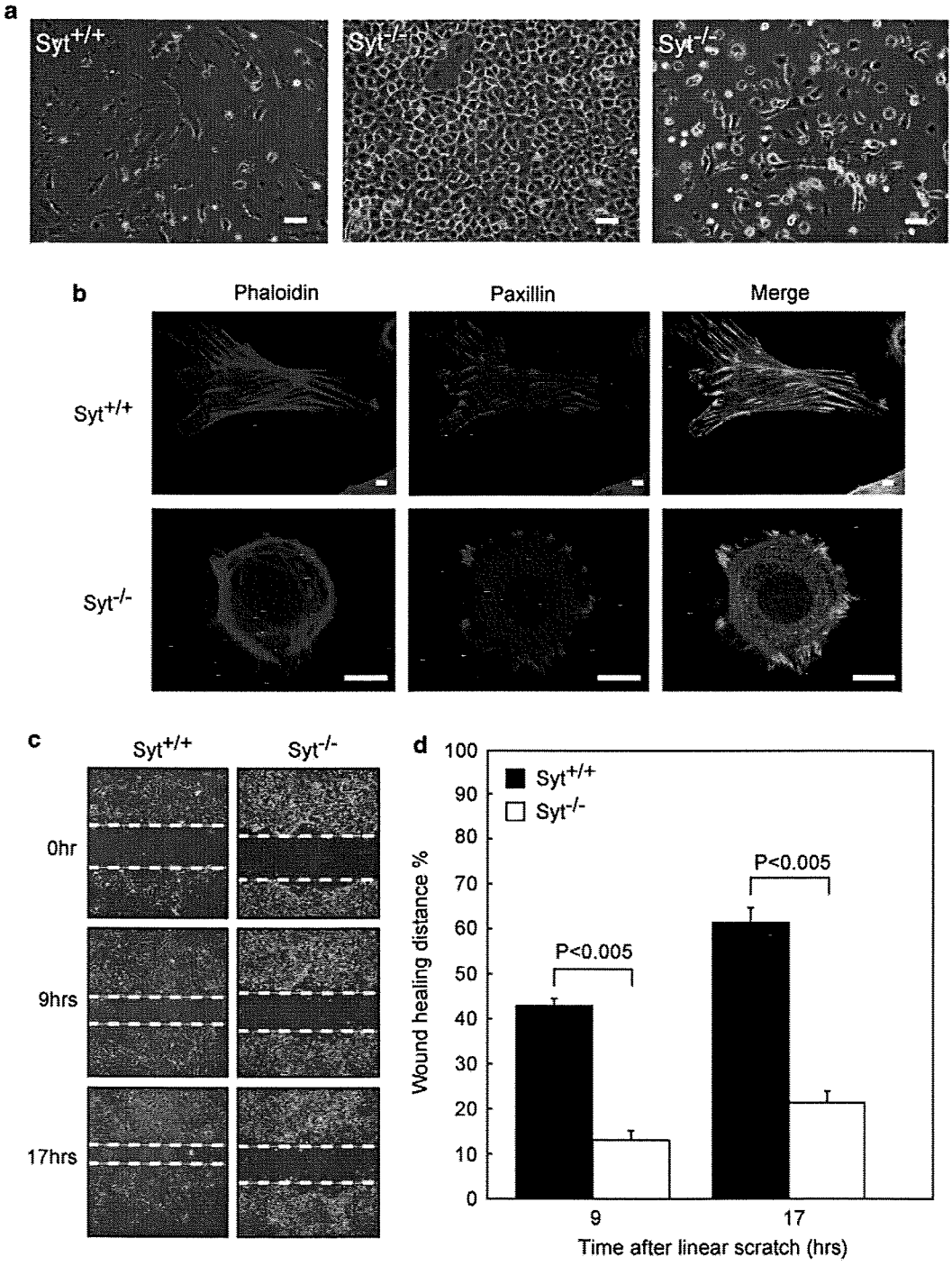

Figure 6 Phenotypical analysis of mouse embryonic fibroblasts established from Syt$^{-/-}$ embryos at E9.75. (**a**) Morphology of wild-type MEFs (right panel) and Syt$^{-/-}$ MEFs (center and left panels) in bright field. Scale bars, 50 μm. (**b**) Representative micrographs of immunocytofluorescence microscopy. Filamentous actin was visualized by phalloidin (right panels) and focal adhesions were visualized by anti-paxillin (center panels) in wild-type (upper panels) and Syt$^{-/-}$ (lower panels) MEFs, respectively. Scale bars, 10 μm. (**c**) Effect of Syt deficiency on motility inhibition. Representative micrographs at the indicated times after wounding. (**d**) Quantitative data from three independent experiments; columns, means, bars, s.d. (Student's *t*-test).

Syt$^{-/-}$ MEFs, especially focusing on participation of p300 in these phenotypes. We performed immunoblot analysis by using lysate from MEFs of the three individual lines (no. 237, no. 239 and no. 244) established from E9.75 embryos. Unexpectedly, unlike the result of the whole embryos, the expression level of p300 did not decrease in Syt $^{-/-}$ MEFs but showed various levels between wild-type and Syt$^{-/-}$ MEFs (Figure 7a). In addition, the expression levels of the other

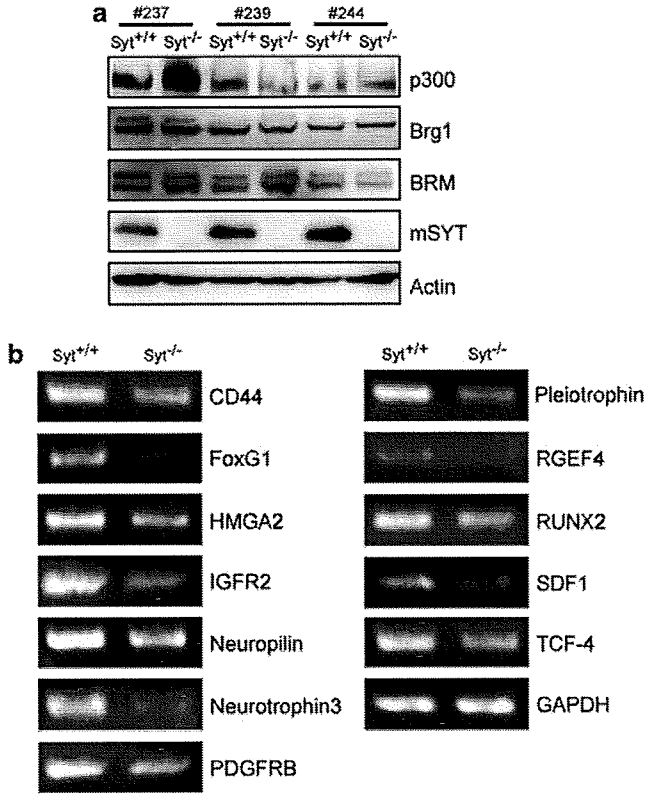

Figure 7 Expression of SYT-interacting proteins and downregulated gene expression in Syt $^{-/-}$ MEFs. (**a**) Immunoblot analysis of SYT-interacting proteins in Syt $^{-/-}$ MEFs. Three independent lines (no. 237, no. 239 and no. 244 indicate maternal mouse number) of MEFs established from E10.5 embryos of wild-type and Syt$^{-/-}$ were subjected to immunoblot analysis for p300, BRG1, hBRM, SYT and actin and are indicated at the right. Thirty micrograms of proteins were loaded in each lane. (**b**) Semi-quantitative RT-PCR analysis of gene expression downregulated in Syt$^{-/-}$ MEFs compared with wild type. Representative data of three independent experiments is shown.

Syt-interacting proteins were not significantly altered between wild-type and Syt$^{-/-}$ MEFs (Figure 7a). These data suggest that the expression level of p300 is not essential for the phenotypes of MEFs, at least, *in vitro*.

To identify the downregulated genes that are related to the phenotypes of Syt$^{-/-}$ MEFs, we performed Gene Chip analysis using wild-type and Syt$^{-/-}$ MEFs established from embryos at E9.75. Of a total of 22 691 genes analyzed, the expression of 2251 genes (5.41%) was significantly decreased by a factor of >3.0 in Syt$^{-/-}$ MEFs compared with wild-type MEFs (Table 2). Structural proteins, such as actin or myosin, matrix proteins, such as collagen, adhesion molecules, such as integrin or cadherin, cell surface receptors, such as CD44 or EphA7, and/or signal transducer, such as RGEF4, were downregulated in Syt$^{-/-}$ MEFs. To confirm these observations, we performed semi-quantitative RT-PCR expression analyses of these putative Syt target genes in other three independent sets of MEFs established from embryos at E9.75, and the microarray results for all 13 genes downregulated in all Syt$^{-/-}$ MEFs were tested (Figure 7b).

Table 2 Selected genes whose expression levels are downregulated in Syt$^{-/-}$ MEFs established from E9.75 embryos compared with wild-type as revealed by Gene Chip analysis

Accession no.	Gene product	Fold change[a]
Structural matrix		
NM_009610	Actin, γ-2, smooth muscle, enteric	−23.82
NM_013607	Myosin heavy polypeptide 11, smooth muscle	−20.66
NM_009925	Procollagen, type X, α-1	−15.77
NM_007733	Procollagen, type XIX, α-1	−13.96
M12233	Actin, α-1, skeletal muscle	−10.94
NM_007729	Procollagen, type XI, α-1	−9.18
AW412729	Procollagen, type XII, α-1	−6.74
AV246911	Procollagen, type V, α-1	−3.34
Transcription factor		
NM_008241	Forkhead box G1	−36.50
NM_010791	Mesenchyme homeobox 1	−22.62
NM_010441	High-mobility group AT-hook 2 (Hmga2)	−11.67
U16321	Transcription factor 4	−6.14
D14636	Runt-related transcription factor 2 (Runx2)	−3.23
Signal transduction		
NM_008742	Neurotrophin 3	−72.10
NM_008809	Platelet-derived growth factor receptor, β-polypeptide	−54.42
NM_015814	Dickkopf homolog 3 (Dkk3)	−29.39
BB623587	Integrin α-8	−27.47
AB021132	Rap guanine nucleotide exchange factor 4	−23.73
NM_008973	Pleiotrophin	−15.29
BB075797	Eph receptor A7	−12.68
NM_008737	Neuropilin	−6.41
BG066982	Natriuretic peptide receptor 3 (Npr3)	−4.93
NM_007631	Cyclin D1	−4.61
NM_130448	Protocadherin 18	−4.41
U04710	Insulin-like growth factor 2 receptor (Igf2r)	−4.01
BC005676	CD44	−3.80
U37029	Integrin β-1D	−3.71
NM_021704	Stromal cell-derived factor 1	−3.20
NM_011519	Syndecan 1	−3.00

[a]Genes are grouped according to the function of the encoded protein. '−' indicates the genes whose expression was downregulated in Syt$^{-/-}$ MEFs compared with that in wild-type MEFs.

DISCUSSION

To understand the biological role of Syt *in vivo*, we generated *Syt*-deficient mice and found that *Syt* deficiency exhibited embryonic lethality, open neural tube and cardiac dysfunction. $Syt^{-/-}$ mutant embryos showed that the defect of ventricular trabeculation and the phenotypes closely resemble those of p300-deficient mice. In fact, the expression levels of p300 were markedly decreased in Syt-deficient mice. Moreover, we isolated $Syt^{-/-}$ MEFs to elucidate the cellular basis of abnormalities in Syt-deficient embryos and showed that Syt participates in the regulation of actin fiber and cell motility.

While this work was in progress, another group reported the establishment of *Syt*-deficient mice, and they reported that Syt deficiency was lethal either through incomplete chorio-allantoic fusion or through a defect in the subsequent process of vascular branching morphogenesis.[17] Surprisingly, placental defect was rarely seen in our $Syt^{-/-}$ mutant embryos. The reason for this discrepancy is not clear, but may be due to differences in targeting strategies or in the genetic background of mice because of using different ES cells.

Syt was found to be essential for early embryogenesis and does not share functional redundancy with other proteins at least in the embryonic stage. In addition, $Syt^{+/-}$ heterozygous mutants showed haplo-insufficient lethality, which is a relatively rare phenotype in gene-disrupted mice. To our knowledge, haplo-insufficient lethality has been observed for p300, Dll4, Vezf1 and ROCK1.[19–21] During embryogenesis, the dosage of Syt may be critical for survival in a certain period *in utero* because newborn $Syt^{+/-}$ mutants lack overt defects. Once such $Syt^{+/-}$ embryos have completed gestation, the reduced Syt dosage does not seem to influence the growth of the newborns.

Normal placental development is initiated by the fusion of the chorionic and allantoic membranes (chorio-allantoic fusion) at E8.5 (8 somites),[22–24] thereby forming the chorionic plate, which is composed of trophoblasts. Through a subsequent process of vascular branching, fetal and maternal blood vessels enter this layer at E9.0, including the development of the placental labyrinth layer, which is made up of syncytiotrophoblasts, and at E10.0, the placenta becomes fully functional. The mutant mice in which the placenta is the only defective organ generally die no sooner than E9.5. In our mutant mice, the major defect begins before E8.5 at least, prior to the usual time of placental lethality. These data suggest that the main reason for our $Syt^{-/-}$ mutant's lethality was not likely to be the placental defect.

Although, morphologically, $Syt^{-/-}$ embryo displayed cardiac abnormalities, the expression levels of genes being essential for cardiac development, including GATA4, MEF2C, Nkx2.5 and so on,[25] were not decreased in $Syt^{-/-}$ embryos. As the proportion of cardiogenesis-specific transcription factor transcripts is very small compared with total embryo mRNA, the difference between wild-type and mutant embryos may not be detectable by this approach.

Interestingly, these embryonic neural and cardiac phenotypes of $Syt^{-/-}$ embryos closely resemble those of p300-deficient mice.[18] On the basis of our data showing that protein levels of p300 were decreased in $Syt^{-/-}$ embryos, Syt may regulate cardiac ventricular maturation through the control of p300 expression.

It was also reported that the SWI/SNF type of chromatin remodeling complex, such as BAF60c and BAF180, has been shown to be required for cardiogenesis.[26,27] In fact, we have found that Syt binds to the complete BAF complex by MALDI-TOF mass spectrometry (T Kimura, unpublished data). Thus, in the absence of Syt, the deregulation of BRG1 together with p300 possibly underlies the defects in the proteins closely related to myofibril formation.

Syt-deficient cells with actin fiber deregulation and suppressed motility might explain the developmental problem. One possible mechanism is that complex formation of SYT and p300, and not only the amount of p300, may regulate cell motility. It was reported that SYT/p300 complex promotes cell adhesion by regulating β1 integrin/fibronectin receptor function.[11] In fact, our Gene Chip analysis showed that integrin β1D and integrin α8, which form heterodimeric transmembrane receptor for fibronectin,[28] were downregulated in $Syt^{-/-}$ MEFs. Thus, p300/SYT complex possibly regulates cell motility through the β1 integrin and/or α8 integrin.

Alternatively, Syt regulated cell migration through the transcriptional regulation of Rap guanine nucleotide exchange factor 4 (now designated as Epac2), which is one of the decreased genes in $Syt^{-/-}$ MEFs. Epac2 was initially characterized as a cAMP-activated GEF for Rap1 and Rap2,[29,30] and as a novel sensor for several pivotal cellular processes, including cell polarization, integrin-mediated cell adhesion, cell migration and cytoskeletal rearrangements through the regulation of Rap, Rho, Ras and Rac.[31–34] As such, we think the possibility that Syt regulates Ras and Rho superfamily through the transcriptional regulation of Epac2.

In this study, we discovered new phenotypes of Syt, such as poor ventricular trabeculation and downregulation of p300 protein in $Syt^{-/-}$ whole embryos. In addition, by the establishment of $Syt^{-/-}$ MEFs, we uncovered that Syt plays an important role in the regulation of cell motility. Thus, $Syt^{-/-}$ MEFs must be one of the useful materials to analyze Syt functions in detail. In future, we will study the association between Syt and malignant human cancer such as synovial sarcoma.

Supplementary Information accompanies the paper on the Laboratory Investigation website (http://www.laboratoryinvestigation.org)

ACKNOWLEDGEMENTS

We thank Dr Ken Sasai (Hokkaido University) and Hiroaki Hiraga (Sapporo Cancer Center) for useful suggestions. This study was supported in part by grants-in-aid from the Ministry of Education, Science, Culture, and Sports, and from the Ministry of Health, Labor, and Welfare; and also by the

YASUDA Medical Research Foundation, by the Suhara Foundation, by the Mochida Memorial Foundation for Medical and Pharmaceutical Research and by the UEHARA Medical Research Foundation.

1. Ladanyi M. Fusions of the SYT and SSX genes in synovial sarcoma. Oncogene 2001;20:5755–5762.
2. Lewis JJ, Antonescu CR, Leung DH, *et al.* Synovial sarcoma: a multivariate analysis of prognostic factors in 112 patients with primary localized tumors of the extremity. J Clin Oncol 2000;18:2087–2094.
3. Clark J, Rocques PJ, Crew AJ, *et al.* Identification of novel genes, SYT and SSX, involved in the t(X;18)(p11.2;q11.2) translocation found in human synovial sarcoma. Nat Genet 1994;7:502–508.
4. dos Santos NR, de Bruijn DR, van Kessel AG. Molecular mechanisms underlying human synovial sarcoma development. Genes Chromosomes Cancer 2001;30:1–14.
5. Thaete C, Brett D, Monaghan P, *et al.* Functional domains of the SYT and SYT–SSX synovial sarcoma translocation proteins and co-localization with the SNF protein BRM in the nucleus. Hum Mol Genet 1999;8:585–591.
6. Brett D, Whitehouse S, Antonson P, *et al.* The SYT protein involved in the t(X;18) synovial sarcoma translocation is a transcriptional activator localized in nuclear bodies. Hum Mol Genet 1997;6:1559–1564.
7. Nagai M, Tanaka S, Tsuda M, *et al.* Analysis of transforming activity of human synovial sarcoma-associated chimeric protein SYT–SSX1 bound to chromatin remodeling factor hBRM/hSNF2 alpha. Proc Natl Acad Sci USA 2001;98:3843–3848.
8. Kato H, Tjernberg A, Zhang W, *et al.* SYT associates with human SNF/SWI complexes and the C-terminal region of its fusion partner SSX1 targets histones. J Biol Chem 2002;277:5498–5505.
9. Ishida M, Tanaka S, Ohki M, *et al.* Transcriptional co-activator activity of SYT is negatively regulated by BRM and Brg1. Genes Cells 2004;9:419–428.
10. de Bruijn DR, dos Santos NR, Thijssen J, *et al.* The synovial sarcoma associated protein SYT interacts with the acute leukemia associated protein AF10. Oncogene 2001;20:3281–3289.
11. Eid JE, Kung AL, Scully R, *et al.* p300 interacts with the nuclear proto-oncoprotein SYT as part of the active control of cell adhesion. Cell 2000;102:839–848.
12. Ito T, Ouchida M, Ito S, *et al.* SYT, a partner of SYT–SSX oncoprotein in synovial sarcomas, interacts with mSin3A, a component of histone deacetylase complex. Lab Invest 2004;84:1484–1490.
13. Nakayama K, Ishida N, Shirane M, *et al.* Mice lacking p27(Kip1) display increased body size, multiple organ hyperplasia, retinal dysplasia, and pituitary tumors. Cell 1996;85:707–720.
14. Sambrook J, Maniatis T, Fritsch EF. Molecular Cloning. A Laboratory Manual, 2nd edn. Cold Spring Harbor Laboratory: NY, 1989.
15. Yang JT, Rayburn H, Hynes RO. Embryonic mesodermal defects in α5 integrin-deficient mice. Development 1993;119:1093–1105.
16. Defilippi P, Truffa G, Stefanuto G, *et al.* Tumor necrosis factor a and interferon g modulate the expression of the vitronectin receptor (integrin h3) in human endothelial cells. J Biol Chem 1991;266: 7638–7645.
17. de Bruijn DR, Peters WJ, Chuva de Sousa Lopes SM, *et al.* Targeted disruption of the synovial sarcoma-associated SS18 gene causes early embryonic lethality and affects PPARBP expression. Hum Mol Genet 2006;15:2936–2944.
18. Yao TP, Oh SP, Fuchs M, *et al.* Gene dosage-dependent embryonic development and proliferation defects in mice lacking the transcriptional integrator p300. Cell 1998;93:361–372.
19. Gale NW, Dominguez MG, Noguera I, *et al.* Haploinsufficiency of delta-like 4 ligand results in embryonic lethality due to major defects in arterial and vascular development. Proc Natl Acad Sci USA 2004;101:15949–15954.
20. Kuhnert F, Campagnolo L, Xiong JW, *et al.* Dosage-dependent requirement for mouse Vezf1 in vascular system development. Dev Biol 2005;283:140–156.
21. Zhang YM, Bo J, Taffet GE, *et al.* Targeted deletion of ROCK1 protects the heart against pressure overload by inhibiting reactive fibrosis. FASEB J 2006;20:916–925.
22. Cross JC. Genetic insights into trophoblast differentiation and placental morphogenesis. Semin Cell Dev Biol 2000;11:105–113.
23. Rossant J, Cross JC. Placental development: lessons from mouse mutants. Nat Rev Genet 2001;2:538–548.
24. Hemberger M, Cross JC. Genes governing placental development. Trends Endocrinol Metab 2001;12:162–168.
25. Srivastava D, Olson EN. A genetic blueprint for cardiac development. Nature 2000;407:221–226.
26. Lickert H, Takeuchi JK, Von Both I, *et al.* Baf60c is essential for function of BAF chromatin remodelling complexes in heart development. Nature 2004;432:107–112.
27. Wang Z, Zhai W, Richardson JA, *et al.* Polybromo protein BAF180 functions in mammalian cardiac chamber maturation. Genes Dev 2004;18:3106–3116.
28. Brakebusch C, Fassler R. β1 integrin function *in vivo*: adhesion, migration and more. Cancer Metastasis Rev 2005;23:403–411.
29. de Rooij J, Zwartkruis FJ, Verheijen MH, *et al.* Epac is a Rap1 guanine nucleotide-exchange factor directly activated by cyclic AMP. Nature 1998;396:474–477.
30. Kawasaki H, Springett GM, Mochizuki N, *et al.* A family of cAMP-binding proteins that directly activate Rap1. Science 1998;282:2275–2279.
31. Bos JL. Linking Rap to cell adhesion. Curr Opin Cell Bio 2005;17: 123–128.
32. Gupta M, Yarwood SJ. MAP1A light chain 2 interacts with exchange protein activated by cyclic AMP 1 (EPAC1) to enhance Rap1 GTPase activity and cell adhesion. J Biol Chem 2005;280: 8109–8116.
33. Del Pozo MA, Alderson NB, Kiosses WB, *et al.* Integrins regulate Rac targeting by internalization of membrane domains. Science 2004;303:839–842.
34. Rangarajan S, Enserink JM, Kuiperij HB, *et al.* Cyclic AMP induces integrin-mediated cell adhesion through Epac and Rap1 upon stimulation of the beta 2-adrenergic receptor. J Cell Biol 2003;160: 487–493.

BIOLOGY OF REPRODUCTION 81, 681–689 (2009)
Published online before print 24 June 2009.
DOI 10.1095/biolreprod.109.076760

Involvement of Phospholipase C-Related Inactive Protein in the Mouse Reproductive System Through the Regulation of Gonadotropin Levels[1]

Miho Matsuda,[3] Koushirou Tsutsumi,[3,4] Takashi Kanematsu,[3] Kiyoko Fukami,[6] Yoshihiro Terada,[4] Tadaomi Takenawa,[7] Keiichi I. Nakayama,[5] and Masato Hirata[2,3]

Laboratory of Molecular and Cellular Biochemistry,[3] Section of Fixed Prosthodontics,[4] Faculty of Dental Science, and Department of Molecular and Cellular Biology,[5] Medical Institute of Bioregulation, Kyushu University, Fukuoka, Japan
Laboratory of Genome and Biosignal,[6] Tokyo University of Pharmacy and Life Science, Tokyo, Japan
Division of Lipid Biochemistry,[7] Kobe University Graduate School of Medicine, Kobe, Japan

ABSTRACT

Phospholipase C-related but catalytically inactive protein (comprising PRIP-1 and PRIP-2 [officially designated PLCL1 and PLCL2]) was first identified in our laboratory, but the biological functions have remained elusive. Therefore, we generated *Plcl1* and *Plcl2* double-knockout mice (*Plcl1*^{tm1Mh}; *Plcl2*^{tm1Tta}) to gain insight into the biological function. Double-knockout mice apparently grew normally and became fertile; however, during animal maintenance, we noticed that mutant couples exhibited decreased litter events and litter size, indicating dysfunction of the reproductive system. Cross-mating experiments to discriminate whether males or females were defective indicated that the cause appeared to be on the female side. Mutant female mice had an apparently smaller uterus by gross anatomical observation and had more estrous days during the cycles. Levels of serum luteinizing hormone (LH) and follicle-stimulating hormone were measured for 5–6 consecutive days and were significantly higher in the mutant, which was also confirmed by examining the secretion of LH from the explant culture of anterior pituitary glands of wild-type and double-knockout mice. These results suggest that through gonadotropin secretion, PRIP plays an important role in female reproduction.

anterior pituitary, estrus cycle, follicle-stimulating hormone, FSH, LH, luteinizing hormone, menstrual cycle, pituitary gland, reproduction system, secretion, signal transduction

INTRODUCTION

Phospholipase C-related but catalytically inactive protein (PRIP [officially designated PLCL]) was first identified as a novel D-*myo*-inositol 1,4,5-trisphosphate [Ins(1,4,5)P_3] binding protein and tentatively named p130 based on molecular size [1]. Subsequent molecular cloning studies revealed that the molecule is similar to phospholipase C-δ1 but catalytically inactive, which is the reason for the revised name, and is expressed predominantly in the brain [2–5]. In an attempt to explore the biological function of PRIP-1 in relation to the binding to Ins(1,4,5)P_3 via its pleckstrin homology (PH) domain [6, 7], we performed serial experiments, first using COS-1 cells stably overexpressing PRIP-1 [8] and then cultured neurons prepared from PRIP-1 knockout (KO) mice (PRIP-1 KO mice [officially designated *Plcl1*^{tm1Mh}]) [9]. The results showed that cells both overexpressing and little-expressing PRIP-1 produced a reduced Ins(1,4,5)P_3-mediated Ca^{2+} increase in cells, probably for different reasons, indicating that the presence of an appropriate amount of PRIP-1 is needed to produce right Ins(1,4,5)P_3-mediated Ca^{2+} signaling. Later, an isoform with relatively broad tissue distribution, including the brain, was reported [10, 11], indicating that PRIP comprises type 1 and 2.

The possible involvement of PRIP in γ-aminobutyric acid type A ($GABA_A$) receptor function was initiated by finding of the binding partners, including the catalytic subunit of protein phosphatase 1 [12–14], protein phosphatase 2A [15], $GABA_A$ receptor-associated protein (GABARAP) [13, 16, 17], and $GABA_A$ receptor β subunits [14, 15]. We also generated *Plcl1* and *Plcl2* (PRIP-1 and -2) double-knockout mice (DKO mice [officially designated *Plcl1*^{tm1Mh} and *Plcl2*^{tm1Tta}, respectively]) to help gain further insight into the functional significance of these proteins in $GABA_A$ receptor signaling and to study further the function of PRIP [18].

During the course of mutant animal maintenance, we noticed that the mutant couples exhibited decreased litter events and litter size, indicating dysfunction of the reproductive system. The hypothalamus-pituitary-gonadal (HPG) axis is central to the reproductive system [19]. The release of gonadotropin-releasing hormone (GnRH) from hypothalamus neurons stimulates the secretion of luteinizing hormone (LH) and follicle-stimulating hormone (FSH) from gonadotrophs in the anterior pituitary glands. The female reproductive system is more vulnerable to gonadotropin dysregulation than the male. LH regulates gonadohormone synthesis and ovulation by mature follicle rupture, and FSH promotes follicle maturation to the preovulatory stage and estrogen release [20].

In this study, we compared DKO mice with control mice in an investigation regarding the processes in the reproduction system influenced by PRIP deficiency. Cross-mating experiments were performed to determine whether male or female is defective in reproduction. We also investigated the estrous cycle by histological analysis of vaginal smears and measured serum levels of gonadotropins during the estrous cycle, followed by the measurements of 17β-estradiol and progesterone. Explant culture of anterior pituitary glands prepared from the control and DKO mice was performed to examine gonadotropin secretion.

[1]Supported by a Grant-in-Aid for Scientific Research from the Ministry of Education, Culture, Science, Sports, and Technology of Japan (to M.M., T.K., and M.H.), by The Uehara Memorial Foundation (to M.H.), and by Japan Diabetes Foundation (to T.K.).
[2]Correspondence: FAX: 81 92 642 6322;
e-mail: hirata1@dent.kyushu-u.ac.jp

Received: 6 February 2009.
First decision: 27 February 2009.
Accepted: 1 June 2009.

eISSN: 1259-7268 http://www.biolreprod.org
ISSN: 0006-3363

MATERIALS AND METHODS

Animals

PRIP-1 and -2 DKO mouse strains and the corresponding wild type (WT) were generated as described previously [15]. In brief, PRIP-1 KO mice and PRIP-2 KO mice back-crossed against the C57BL/6J (Charles River Laboratories Japan, Inc.) background were crossed to generate a DKO mouse strain and corresponding WT. Homozygous DKO and WT mice were intercrossed to obtain the required number of mice, and only F1 and F2 generations of both genotypes were used for experiments. The handling of mice and all procedures were approved by the Animal Care Committee of Kyushu University, following the guidelines of the Japanese Council on Animal Care.

Mouse Fertility Assessment

WT or DKO females aged 12 wk were mated with age-matched WT or DKO males. Once found to be pregnant, female mice were isolated until they gave birth. After counting the number of pups, the female mice were returned to mating cages the next day. This continued for 4 mo.

Determination of Estrous Cycle

The pattern of estrous cycles was determined using 3-mo-old female mice for 28 consecutive days. Animals were maintained under 12L:12D (lights on from 800 to 2000 h) and vaginal smears were collected at the same time (1700 h) every day, by flushing the vagina with PBS. Aliquots of collected smears were mounted on glass slides to stain with Giemsa solution. Stained cell samples were examined under a microscope with a magnification of 100×. When nucleated cells or cornified cells were dominant in the smear, the mice were assigned to be in proestrus or estrus. Metestrus or diestrus was assessed by the presence of a multitude of leukocytes, and all of these criteria are based on those described previously [21].

Measurement of Hormone Levels

About 300–400 μl of blood samples were collected every day at 1700 h for 5 or 6 consecutive days from retinal blood vessels of 3-mo-old mice, and sera were prepared. Sera (50 μl) were used for the measurement of LH (sensitivity >0.2 ng/ml) and FSH (sensitivity >0.2 ng/ml) concentrations by ELISA using the respective kits (Endocrine Technologies, Inc.) according to the manufacturer's protocol. Sera (50 μl) were also used for the measurement of progesterone (sensitivity >0.1 ng/ml) and 17β-estradiol (sensitivity >3 pg/ml) by the respective ELISA kits (Endocrine Technologies, Inc.) according to the manufacturer's protocol. Anterior pituitary glands, isolated from 3-mo-old mice of each genotype, were homogenized by a Teflon-pestle homogenizer (Nippon Rikagaku Kikai) in PBS containing 0.5% Triton, followed by a centrifugation at 50 000 × *g* for 10 min. The extracts (40 μg) were used for the measurement of the amount of LH and FSH using a kit as described above.

Explant of Pituitary Gland

Anterior lobes of the pituitary glands were carefully isolated free from intermediate and posterior lobes under a stereoscopic microscope (Olympus) from 3-mo-old female mice of each genotype immediately after decapitation, followed by cultivation according to the method described by John et al. [22]. After dividing the isolated anterior pituitary gland into four segments of equal size, the segments were incubated with 100 μl of Eagle balanced salt solution (Sigma) in a 96-well culture plate for 3 h at 37°C, with medium changes every hour. The segments were then stimulated with fresh medium containing 40 nM buserelin (des-Gly_{10}-[D-Ser{t-Bu}$_6$]-LH-RH ethylamide; Sigma) or high K^+ buffer (80 mM KCl, 45 mM NaCl, 1.2 mM KH_2PO_4, 1.3 mM $MgSO_4$, 20 mM $NaHCO_3$, 10 mM Hepes [pH 7.4], and 2.4 mM $CaCl_2$) for 5, 15, 30, and 60 min. The incubation medium was collected carefully at the time indicated without sucking up the tissue segments with the pipet, and the segments were supplemented with fresh medium with or without stimulants. Medium collected was cleared by a centrifugation at 10 000 × *g* for 5 min and was then assayed for secreted LH by ELISA.

Immunoblotting

Hypothalamic regions, anterior-pituitary glands, testes, and ovaries isolated from 3-mo-old mice of each genotype were extracted with lysis buffer (25 mM Tris-HCl [pH 7.5], 150 mM NaCl, 1% Triton, and 5 mM EDTA). Total cell lysates were separated by SDS-PAGE, followed by transfer to polyvinyldifluoride membrane and immunoblotting with antibodies against PRIP-1 (1:1000) [15], PRIP-2 (1:1000) [15], β-subunit of LH (1:1000; Biogenesis). β-subunit of FSH (1:1000; Biogenesis), LH receptor (LHR; 1:1000; Santa Cruz Biotechnology), FSH receptor (FSHR; 1:300; Santa Cruz Biotechnology), β-tubulin (1:2000; Upstate), and β-actin (Sigma). Blots were developed with horseradish peroxidase-coupled secondary antibodies and visualized using the ECL system (Amersham Biosciences). Density was quantified by an Image Gauge software (version 3.0; Fujifilm) and shown as a relative value after normalizing with that of β-tubulin or β-actin in each experiment.

PCR Conditions

Mouse anterior pituitary glands (3-mo-old) were isolated and homogenized for total RNA extraction. Total RNA was extracted by an illustra RNAspin Mini RNA Isolation kit (GE Healthcare) according to the manufacturer's instructions. After cDNA synthesis using total RNA (1 μg) with ReverTra Ace (Toyobo), PCR amplifications were performed in 50 μl with 2–5 μl of obtained cDNA and 200 nM of each primer by Platinum PCR SuperMix High Fidelity kit (Invitrogen) according to the manufacturer's protocols. Primer pairs used for semiquantitative RT–PCR were as follows: mouse LH fwd: 5′-GCTG CTGAGCCCAAGTGTG, and rev: 5′-ATTGGTTGAGTCCTGGGACC; mouse FSH fwd: 5′-AGACAGCTGACTGCACAGG, and rev: 5′-TTACGGTCTCGTATACCAGC; mouse glyceraldehyde-3-phosphate dehydrogenase (G3PDH) fwd: 5′-ACCACAGTCCATGCCATCAC, and rev: 5′-TCCACCACCCTGTTGCTGTA. Thermal-cycling conditions were 25 cycles of 30 sec at 94°C, 30 sec at 58°C, and 20 sec at 72°C for LH and FSH amplification and 25 cycles of 30 sec at 94°C, 30 sec at 62°C, and 30 sec at 72°C for the G3PDH. Quantitative RT-PCR analysis was performed with a TaqMan gene expression assay (Applied Biosystems) on a 7500 real-time PCR system (Applied Biosystems). Thermal cycling conditions were 40 cycles of 15 sec at 95°C and 1 min at 60°C.

Statistical Analysis

Data are presented as the mean ± SEM of at least three independent experiments in each figure. Student *t*-tests were used and significance is represented by * or ** for $P < 0.05$ or $P < 0.01$, respectively.

RESULTS

Phenotype of DKO Mice Related to Reproduction

We generated *Plcl1* and *Plcl2* (PRIP-1 and -2) DKO mice [15], but we soon noticed that it was hard to maintain the deficient mice strain because of the decreased number of pups born and the decreased frequency of litter; therefore, we systematically examined the fertility of the deficient mice from the age of 12 wk for 4 mo using four and seven pairs of WT and DKO, respectively. As shown in Table 1 and Figure 1, the litter size of the WT pair was 6–8.8, while that of the DKO pair was 0–7. The average interval between litters of WT pairs was 26.2 days, whereas that of DKO was 35.2 days, indicating fewer pups per litter and a prolonged interval between litters. Therefore, the total number of pups born during the period examined was 18–35 and 0–20 for WT and DKO pairs, respectively. One of the mutant pairs delivered no pups during the period examined (Table 1). To determine whether males or females were defective, cross-mating experiments were performed using five or six cross pairs; male DKO exhibited normal fertility, whereas female DKO paired with male WT showed a decreased number of pups during the period examined (Fig. 1D), which was very similar to those observed with DKO pairs, indicating that the reproductive defect was in females.

Gross anatomical observations of the reproductive organs as well as the body weight were then performed (Fig. 2). The only difference in gross anatomy among organs examined from both genotypes at the age of 6 mo was in the uterus. As shown in Figure 2E, DKO mice exhibited a smaller uterus on the whole, but the wall thickness showed little difference, and histological analysis of the uterus showed no significant difference in mucous, muscle, and adventitial layers between WT and DKO

TABLE 1. Distribution of pups.

Genotype[a]		No. of pups per litter					
Female	Male	First delivery	Second delivery	Third delivery	Fourth delivery	Average	Total pups
WT	WT	9	8	9	9	8.8	35
		8	4	6		6	18
		7	10	7	10	8.5	34
		4	6	9	10	7.3	29
DKO	DKO	6	8	1	5	5	20
		9	3	7		6.3	19
		6				6	6
		7				7	7
		7	1			4	8
		5				5	5
		0				0	0

[a] WT or DKO females at the age of 12 wk were mated with age- and genotype-matched males for four months (n = 4 or 7, respectively).

(Supplemental Fig. S1; all Supplemental Figures are available online at www.biolreprod.org). It was noteworthy that no difference in the size of the uterus between two genotypes was observed in mice up to the age of at least 12 wk, but then the growth appeared to be downregulated with age, indicating that a small uterus in DKO mice is not innate, but becomes overt after puberty.

In order to further characterize the reproductive physiology of DKO mice, we examined the estrous cycle in mice by histological analysis of vaginal smears. Five mice of each genotype at the age of 3 mo were analyzed every day at 1700 h for 28 days (Fig. 3). WT mice showed relatively regular estrous cycles lasting 4 to 5 days, i.e., 24.3% of the days (34/140 days) were estrous days. DKO females also showed cyclic estrus, but the estrous days were apparently increased (41.4%, 58/140 days), indicating the dysregulation of gonadotropin levels in DKO mice.

Effect of PRIP Deficiency on Gonadotropin Secretion

We first examined the expression of PRIP in tissues involved in gonadotropin secretion according to the HPG axis. Both PRIP-1 and -2 were found to be expressed in the hypothalamus and anterior pituitary gland, but to a smaller extent in the testis or ovary (Fig. 4). Figure 4 also showed no expression of PRIP-1 and -2 in DKO mice.

We then measured serum concentrations of LH and FSH in females of both genotypes at the age of 3 mo for 5 or 6 days because their average estrous cycles were 4–5 days. WT mice exhibited an LH surge for a day, albeit with variable maximum levels (Fig. 5A). On the other hand, DKO mice appeared to have consistently higher basal LH levels, and some of the deficient mice showed lasting high levels of LH, showing no distinct LH surge (Fig. 5A). The average level of all LH concentrations measured with DKO females was about twice as much as those seen with WT mice (Fig. 5A, right). A similar

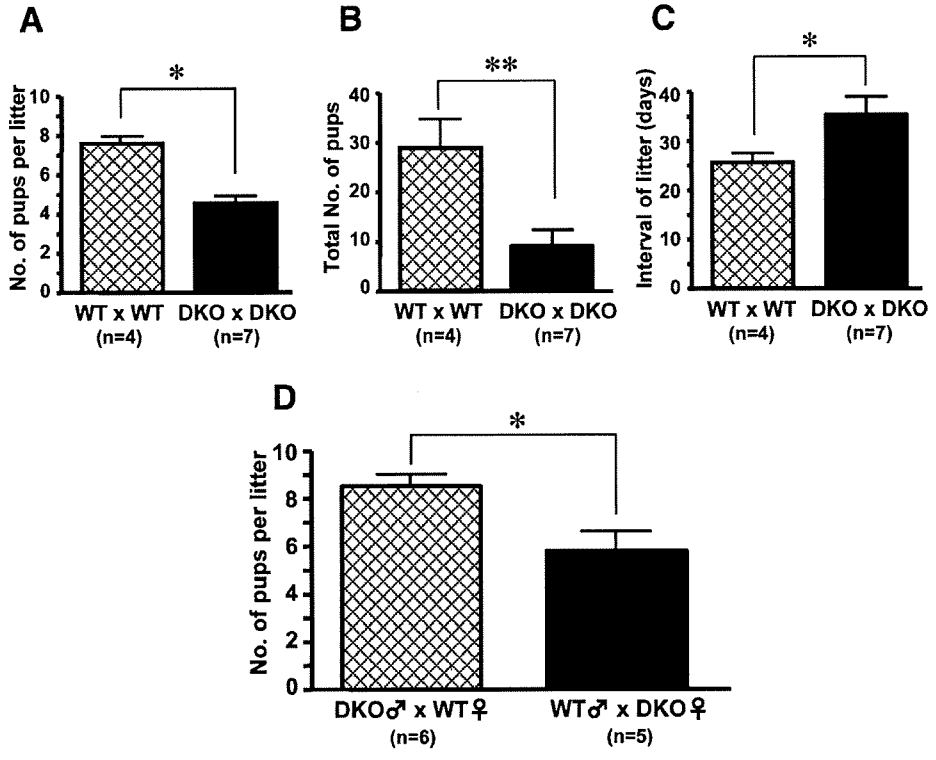

FIG. 1. PRIP-deficient mouse fertility in continuous mating. WT or DKO females at the age of 12 wk were mated with age- and genotype-matched males for 4 mo (n = 4 or 7, respectively). Number of pups per litter (**A**), total number of pups (**B**), and litter interval (**C**) are shown. In **D**, DKO males were continuously mated with WT females for 4 mo (n = 6) and vice versa (n = 5), and only the mean number of pups per litter is shown. Data are the mean ± SEM of 4–7 pairs (Student *t*-test, $*P < 0.05$, $**P < 0.01$).

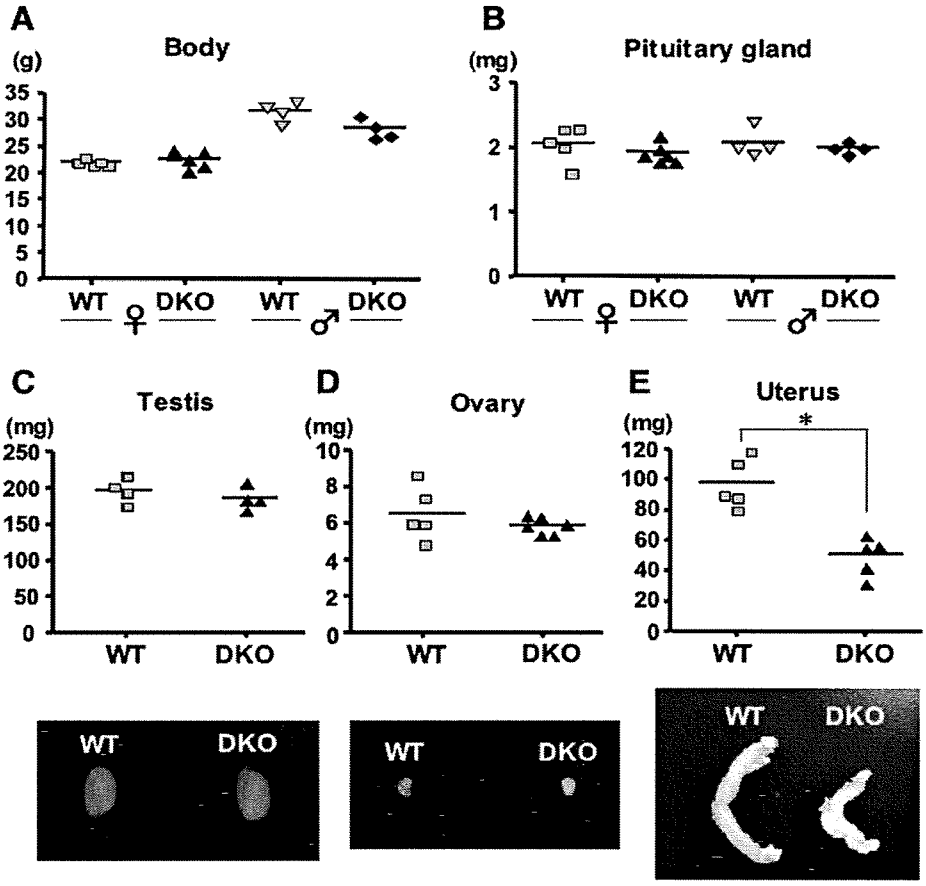

FIG. 2. Wet weights of WT and DKO reproductive organs. Bodies (A) were weighed, and pituitary gland (B), testis (C), ovary (D), and uterus (E) were isolated and carefully freed from connective tissues from 6-mo-old mice at the diestrous period in both genotypes. Four males and five (in some cases six) females of WT and DKO mice were examined. Typical pictures of testis, ovary, and uterus are also shown. $^*P < 0.05$.

pattern of increased levels of FSH was also observed in DKO females (Fig. 5B).

We further investigated the basal and stimulation-dependent secretion of LH from isolated mouse anterior lobes of pituitary glands in vitro. As described in *Materials and Methods*, isolated anterior lobes of pituitary glands prepared from WT or DKO mice at the age of 3 mo were incubated alone or with stimulants (buserelin, an analog of GnRH and high K^+) for the periods indicated. As shown in Figure 6, the lobes from DKO mice secreted more LH in response to both buserelin and high K^+ solution, and furthermore, it was noteworthy that basal secretion of LH without any stimulation was also higher in DKO mice. The basal secretion of FSH was also elevated in the mutant mice (data not shown).

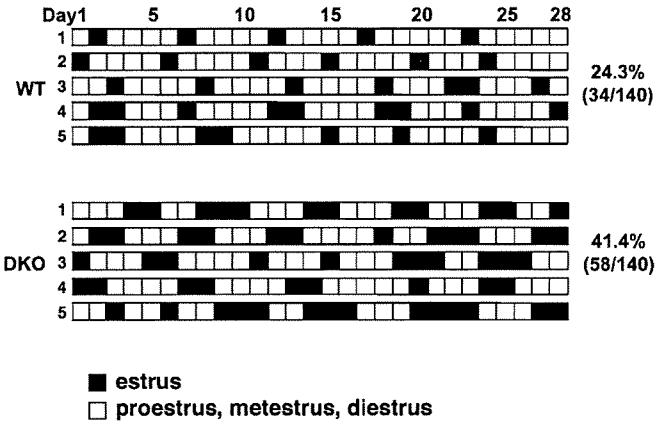

FIG. 3. Estrous cycles in WT and DKO females. Vaginal smears were taken from five WT and five DKO females every day at 1700 h for 28 consecutive days, followed by histological analysis. The numbers shown on the left indicate individual mice. Closed squares show estrous days, and proestrous, metestrous, and diestrous days are shown as open squares. Percentage shown on the right shows estrous days per days accumulated from five mice at the age of 3 mo.

To analyze the production of LH and FSH at both mRNA and protein levels in the anterior lobes of pituitary glands from both genotypes, quantitative RT-PCR, immunoblotting, and ELISA analyses were performed using the total RNA or tissue extracts. As shown in Figure 7, LH and FSH at protein level were decreased in DKO compared to those in WT (Fig. 7B), whereas little changes were observed in mRNA level (Fig. 7A), indicating that LH and FSH are constantly secreted more in DKO mice, but the transcriptions are unchanged.

Elevated serum levels of LH and FSH may affect the secretion of related hormones from the target tissues, such as the ovary and testis. We then examined serum levels of progesterone and 17β-estradiol secreted from the ovary using the same blood samples collected for LH and FSH assays. The mean values of several mice with either genotype for 5–6 days are shown in Figure 8, A and B. The serum levels of progesterone in DKO mice were apparently lower than those of WT, whereas the levels of 17β-estradiol in DKO mice showed statistically little difference from those of WT mice, but with slightly lower levels (Fig. 8, A and B). Histological analysis of the ovaries for the number of corpus luteum was performed, showing little difference (Supplemental Fig. S2). The expression of the gonadotropin receptors LHR and FSHR in WT and DKO ovary extracts was also examined by immunoblotting using the respective anti-receptor antibody. Clear bands with a molecular size of 85 kD and 75 kD for LHR and FSHR,